System Integration, Parametric Study and Temperature Prediction Using Machine Learning in Direct Energy Deposition

by

Erfan Bayat

B.Sc., Amirkabir Univeristy of Technology, 2020

A THESIS SUBMITTED IN PARTIAL FULFILLMENT OF
THE REQUIREMENTS FOR THE DEGREE OF

MASTER OF APPLIED SCIENCE

in

The Faculty of Graduate and Postdoctoral Studies

(Mechanical Engineering)

THE UNIVERSITY OF BRITISH COLUMBIA

(Vancouver)

April 2023

The following individuals certify that they have read, and recommend to the Faculty of Graduate and Postdoctoral Studies for acceptance, the thesis entitled:

System Integration, Parametric Study and Temperature Prediction Using Machine Learning in Direct Energy Deposition

submitted by Erfan Bayat in partial fulfilment of the requirements for

the degree of Master of Applied Science

in Mechanical Engineering

Examining Committee:

Xiaoliang Jin, Associate Professor, Mechanical Engineering, UBC
Supervisor

Adam Clare, Professor, Mechanical Engineering, UBC
Supervisory Committee Member

Ryozo Nagamune, Professor, Mechanical Engineering, UBC
Supervisory Committee Member

Abstract

In Direct Energy Deposition (DED), the melt pool temperature is a critical control parameter that affects deposition rate, porosity formation, residual stress, and microstructure in the final parts. In this thesis, a data-driven approach using Machine Learning (ML) models is used to predict the melt pool temperature using experimental data. This thesis presents the integration of the laser-based DED system using metal powder feedstock, the determination of the process parameter window for the setup, and the development of an ML pipeline to predict the melt pool temperature based on its history.

In the system integration for the DED system, a laser generator, powder feeder, deposition head, and sensors (i.e., an IR camera and a 2-wavelength pyrometer) were integrated into an existing 3-axis motion stage. Python-based software was developed to control the laser generator and to read data from the sensors. The software calibrates the IR camera's temperature, which is highly dependent on the emissivity, by leveraging the data from the 2-wavelength pyrometer. To determine the process parameter window, 150 single-layer clads were deposited; clads' cross-sections were polished and etched and optical microscopy was used to measure the clad's height, melt pool's depth, and dilution ratio. Analysis was conducted on the correlation of the process parameters, laser power, scan speed, flow rate, and the measured properties of the clads. The process parameters with the minimal dilution of (5-25%) were selected to obtain clads with proper geometry and bonding to the substrate.

Finally, the temperature data of a 6-layer thin wall with the obtained process parameters were used to train several ML models, including Dense Neural Networks (DNN), 1-Dimensional Convolutional Neural Networks (1D-CNN), Recurrent Neural Networks (RNN), Long Short-Term Memory (LSTM), and Gated Recurrent Unit (GRU). LSTM shows better performance among these models; therefore it was implemented in the ML pipeline for temperature prediction. The Model can predict the trend and fluctuations of the melt pool temperature with higher accuracy compared to the existing models for melt pool temperature prediction in the DED process.

Lay Summary

Laser-based Direct Energy Deposition is an additive manufacturing method using a laser beam to melt metal powders for printing a part. This process gained attention in recent years due to its ability to produce parts with complex geometries and unique material properties. This thesis focuses on the integration of a DED system (i.e., laser generator, powder feeder, and deposition head) and sensors, including an IR camera and a 2-wavelength pyrometer, into an existing 3-axis motion stage. Subsequently, the process parameter window for the setup is determined based on the analysis of the cross-section of clads. The DED process is a multi-physics phenomenon in which melting and solidification are happening very fast and it makes the process hard to model based on analytical and numerical approaches. Therefore, a machine learning pipeline is developed to predict the temperature of the melt pool based on its temperature history gathered from the experiment.

Preface

This thesis entitled *System Integration, Parametric Study and Temperature Prediction Using Machine Learning in Direct Energy Deposition* presents the work of the author, Erfan Bayat under the supervision of Dr. Xiaoliang Jin throughout the Master of Applied Science (MASc) program at UBC Mechanical Engineering.

The integration of the DED hardware and software systems described in Chapter 3 is developed based on the previous work by AO Chio and Aashkaran Dhillon. The parametric study of process parameters in Chapter 4 and the machine learning model for temperature prediction in Chapter 5 is the original work done by the author.

Table of Contents

List of Tables

List of Figures

List of Symbols

A_1	Area of the clad above the substrate
A_2	Area of the clad below the substrate
$a^{<t>}$	Hidden states in the sequence models at time (t)
b_a	Bias term for hidden states
b_c	Bias term for the memory content in the GRU and LSTM model
b_r	Bias term for the relevance gate in the GRU model
b_u	Bias term for the update gate in the GRU and LSTM model
b_y	Bias term for outputs
$C^{<t>}$	Memory content in the GRU and LSTM model
$\tilde{C}^{<t>}$	Possible candidate for the memory content
T	Temperature
W_{aa}	Weight matrix for the hidden states in the RNN model
W_{ax}	Weight matrix for the inputs in the RNN model
W_{ay}	Weight matrix for the outputs in the RNN model
W_c	Weight matrix for the cell's memory content
W_f	Weight matrix for the forget gate
W_o	Weight matrix for the output gate
W_r	Weight matrix for the relevance gate
W_u	Weight matrix for the update gate
$X^{<t>}$	Input parameter to the ML model at each time
y	Temperature value measured by the pyrometer (True value)
$\hat{y}^{<t>}$	Predicted temperature value by the machine learning model at time (t)
α	Absorptivity
Γ_r	Relevance gate
Γ_u	Update gate
η	Dilution ratio
λ	radiation wavelength
μ	mean value
ρ	Reflectivity
σ	standard deviation
τ	Transmissivity
Φ	Heat flux reaching to the surface of a body
$\Phi_{\aleph}$	Absorbed heat flux from the surface of a body
Φ_{ρ}	Reflected heat flux from the surface of a body
Φ_{τ}	Transmitted heat flux from the surface of a body

Abbreviations

1D	1 Dimensional
3D	3 Dimensional
AM	Additive Manufacturing
ASTM	American Society of Testing and Materials
CAD	Computer Aided Design
CAGR	Compound Annual Growth Rate
CNN	Convolutional Neural Network
CPU	Central Processing Unit
DED	Direct Energy Deposition
DLD	Direct Laser Deposition
DNN	Dense Neural Network
FDM	Finite Difference Method
FEM	Finite Element Method
FVM	Finite Volume Method
GPU	Graphics Processing Unit
GRU	Gated Recurrent Unit
GUI	Graphical User Interface
IR	Infrared
LSTM	Long Short-Term Memory
MAE	Mean Absolute Error
ML	Machine Learning
RNN	Recurrent Neural Network
RPM	Round Per Minute
SGD	Stochastic Gradient Descent
SS	Stainless Steel

Acknowledgements

First and foremost, my immense gratitude to Dr. Xiaoliang Jin and Dr. Adam Clare for their insight, guidance, and continuous support throughout my masters program, without them this thesis would not have been completed. I am particularly grateful to them for giving me time and academic freedom to explore new ideas, try different ways, and think independently.

Many thanks to the committee members, Dr. Adam Clare and Dr. Ryozo Nagamune, for reading this document, assessing my work, and their helpful feedback.

I would like to thank all my dear friends and lab mates, Reza, Farshad and Sajjad with whom I enjoyed invaluable moments of company and conversation which truly made this journey a memorable experience.

The most important of all, I am sincerely thankful to my parents and brother who provided me with their loving support.

Chapter 1

Introduction

In recent years, there have been continuous advancements in the industry and increased demand for the production of more complex parts, components with functionally graded materials, and waste reduction across a range of sectors like aerospace, biomedical, automobile, etc. As a result, Additive Manufacturing (AM) has been increasingly used in the era of Industry 4.0. The AM market has seen a significant growth rate with a Compound Annual Growth Rate (CAGR) of 19.5% and is expected to reach $11.8 B. by 2028 [21]; these numbers are indicating a growing trend for the implementation of AM in various industrial sectors for manufacturing.

The American Society of Testing and Materials (ASTM) standard F2792 defines AM as "the process of joining material to make objects from 3D model data, usually layer upon layer" [40]. There are many approaches in AM, and Direct Energy Deposition (DED) is a widely used process that uses a laser beam (known as Direct Laser Deposition (DLD)), electron beam, or plasma/electric arc as the energy source to melt feedstock materials, either in powder or wire form, to print a part layer by layer from the Computer-Aided Design (CAD) model.

Despite the many advantages of metal AM, there are still limitations to its full implementation in critical sectors such as aerospace and defense, medical devices, automation, and precision manufacturing. Defects, including porosity, cracks, incomplete fusion, non-uniform material properties, and poor surface finish, remain major challenges of AM in these fields. To address these issues, various control strategies on the process parameters are utilized in DED; among them, laser power, scan speed, and powder flow rate have the greatest impact on the melt pool size, temperature, and the quality of the printed clad [5, 24]. Therefore, it is essential to determine the process window that ensures the accepted quality of the printed parts.

One major challenge in improving the metal AM process and making it more accessible to critical sectors is the inherent complexity of the process that makes accurate modeling or simulation difficult because of the multiple physical phenomena, like melting, solidification, etc., occurring during deposition process [35]. Numerous research studies are currently underway to develop appropriate analytical and numerical models for the metal AM process. Analytical models can provide quick predictions and can be utilized for optimizations. However, when developing such models, it is necessary to establish certain assumptions to simplify the modeling, which can introduce discrepancies between the formulation and reality. The Finite Element Method (FEM), Finite Volume Method (FVM), and Finite Difference Method (FDM) are numerical approaches utilized for modeling the AM process. These models also encounter the issue of discrepancies between the model and experiment, and in addition, simulations can take up to weeks to complete. Nevertheless, numerical models provide valuable insights into the entire process for each desired location in the printed part. Given these challenges, data-driven approaches are increasingly being recognized as promising solutions to various challenges in AM. These models leverage experimental data collected during experiments and utilize Machine Learning (ML) techniques to uncover hidden correlations within the data. While training time for complex models can take from several hours up to several days, once trained, they can do predictions immediately over the input data. Furthermore, since they are trained based on experimental data, the previously mentioned discrepancy issues can be resolved. Given the current state of artificial intelligence (AI) and ML, these models are increasingly being utilized for in-process monitoring, defect detection, and other applications in AM.

The focus of this thesis is to identify the process window and train an ML-based temperature predictor model for the in-house DED system. This system was developed by integrating various DED components, including the deposition head, powder delivery system, and laser generator, onto an existing 3-axis motion stage.

Since online monitoring of the melt pool can provide valuable insights into the manufacturing process and help to detect defects, an IR camera, and a 2-wavelength pyrometer are integrated into the setup to provide information about the morphology and temperature of the melt pool, respectively. These melt pool data can be used to optimize the process parameters and develop process control strategies for improving the overall quality of the process. In order to implement feedback control in the setup, open-source software was developed in Python that can control the laser generator and gather data from the IR camera and the pyrometer. This software leverages the temperature readings from the pyrometer to calibrate the IR camera data, which is highly dependent on the emissivity of the object. As the software is open-source, it allows for the implementation of more advanced control algorithms and processing techniques in the future.

In order to achieve high-quality single-layer clads, 150 experiments were conducted with variations in the main process parameters, including laser power, scan speed, and powder flow rate. Following the etching of the cross-section of each clad, the proper process parameters were determined based on the factors such as minimal dilution, strong bonding, and proper clad geometry. The proposed process parameters were utilized to print a part consisting of multiple layers.

As previously mentioned, AM is limited by the challenge of accurately modeling and predicting the morphology and temperature of the melt pool. This is due to the high computational cost of simulations and the difficulty of developing precise analytical models. Current research is exploring the use of vision systems to monitor the morphology and temperature distribution of the melt pool, as a means to ensure high-quality parts. However, while these studies are ongoing, there are few investigations focused specifically on online prediction of melt pool temperature using data-driven approaches. This represents an area of potential growth and innovation in the field of AM. Due to the latency between changes in laser power and variations in melt pool temperature, it is beneficial to predict the future temperature and adjust the power accordingly in advance to obtain a more uniform deposition and microstructure in the clads. This strategy can compensate for the latency and minimize delays in controlling DED processes, leading to improved efficiency and quality in the manufacturing process. To address this challenge, an ML pipeline that leverages the melt pool's temperature history to predict future temperature changes is developed in this thesis. Several ML models, including Dense Neural Networks (DNN), 1D Convolution Neural Networks (1D-CNN) model, Recurrent Neural Networks (RNN), Long Short-Term Memory (LSTM), and Gated Recurrent Unit (GRU) were tested to determine the best model to be integrated into the pipeline. The performance of the ML model in this thesis has demonstrated significantly better performance compared to the existing models in the literature.

The thesis is organized as follows; chapter 2 of the thesis provides a comprehensive literature review on the challenges of the DED process, DED process window, post-process characterization, and online monitoring, as well as the data-driven approaches used in the DED process for process monitoring and prediction. Chapter 3 includes the integration of the DED components and sensors into the motion stage and the development of control software. Chapter 4 presents the process of determining the process parameter window that results in optimal dilution and clad geometry. Chapter 5 provides the ML pipeline and approaches utilized for melt pool temperature prediction. In conclusion, Chapter 6 provides an overview of the findings and presents possible future directions for the research. Figure 1.1 shows the flowchart of the thesis in detail.

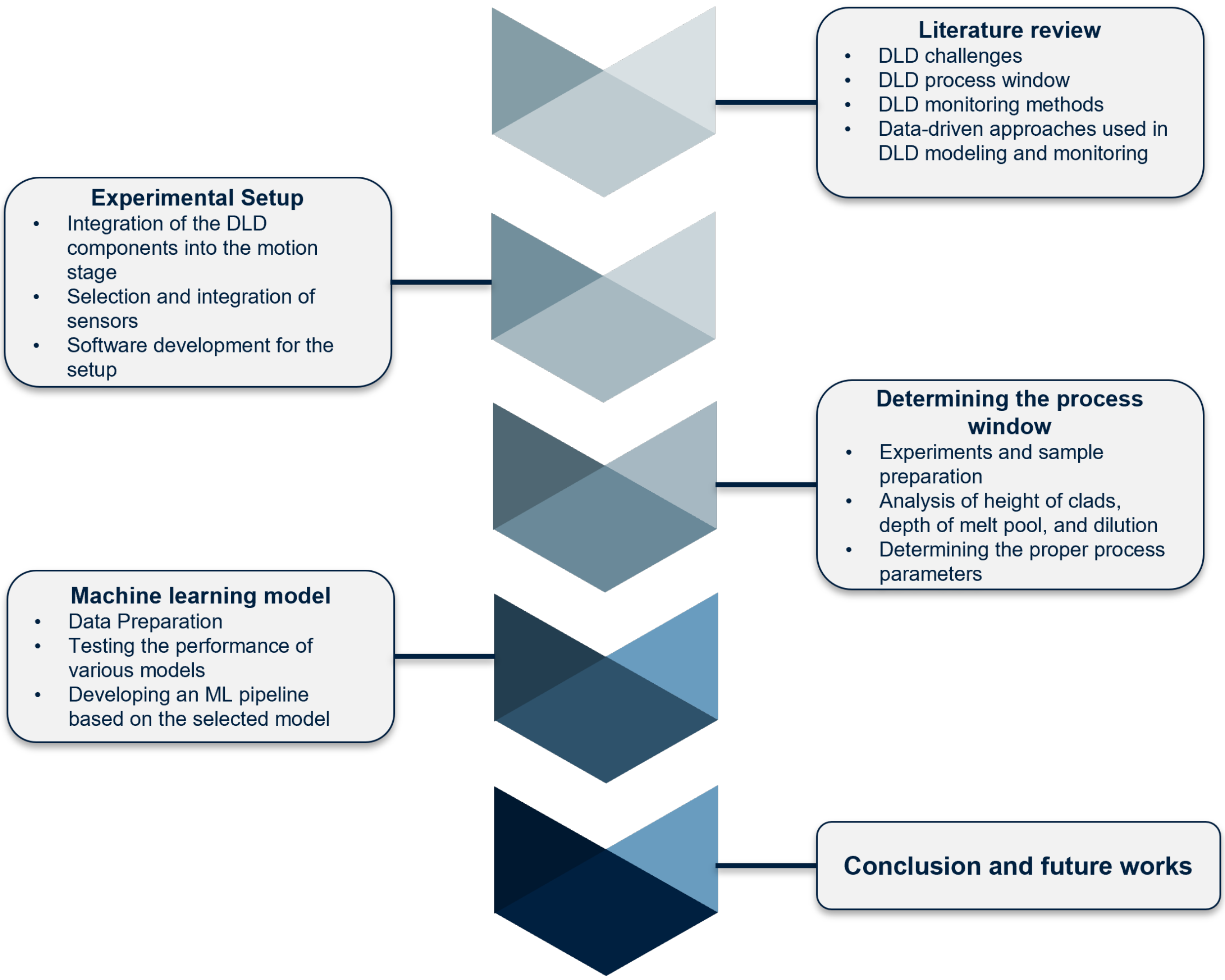

Figure 1.1: Thesis flowchart.

Chapter 2

Literature Review

This section provides a literature review on the laser-based DED process that is covering research on the challenges and defects associated with DED, process monitoring, determining the process parameter window, and data-driven modeling.

2.1 Powder DED

The powder-based DED process was first patented by Jeantette et al. in 1996 [15]. As a subcategory of AM, this technique involves delivering feedstock material in the form of powder to a melt pool created by a laser beam, electron beam, or plasma/electric arc. In 1998, Atwood et al. demonstrated that Laser Engineering Net Shaping (LENS^{TM}) can produce parts with an accuracy of 0.05 mm [3]. In the laser-based DED process using powder feedstock, the metal powder is conveyed to the melt pool via the carrier gas, and the laser melts the metal powder; meanwhile, shield gas that is the same type as the carrier gas is used to protect the melt pool from oxidation. The melted metal powder is subsequently deposited onto the substrate when the deposition head is moving and it cools down rapidly and solidifies. This layer-by-layer process continues until the part is printed. This technique is promising in terms of accuracy, and a wide range of materials are used in AM, including low-alloy steel, stainless steel [45], nickel-based alloys [22], and titanium alloys [17]. Figure 2.1 shows the configuration of the deposition head and the deposition process.

2.2 Powder DED Applications

The DED process finds applications in a wide range of sectors, including:

- **Manufacturing of complex parts:** Layer-by-layer printing of the parts gives the freedom to produce parts with complex geometries with a wide range of materials. DED provides the opportunity to produce lattice structures, molds, and parts with complex geometries that can be used in various sectors, like medical devices, aerospace, etc. [32, 43]

- **Repair:** DED can be a useful method for repairing large and expensive components that have been damaged or worn. This technology can repair the part in its original location without the need for remanufacturing, resulting in more sustainable solutions and cost reduction [28]

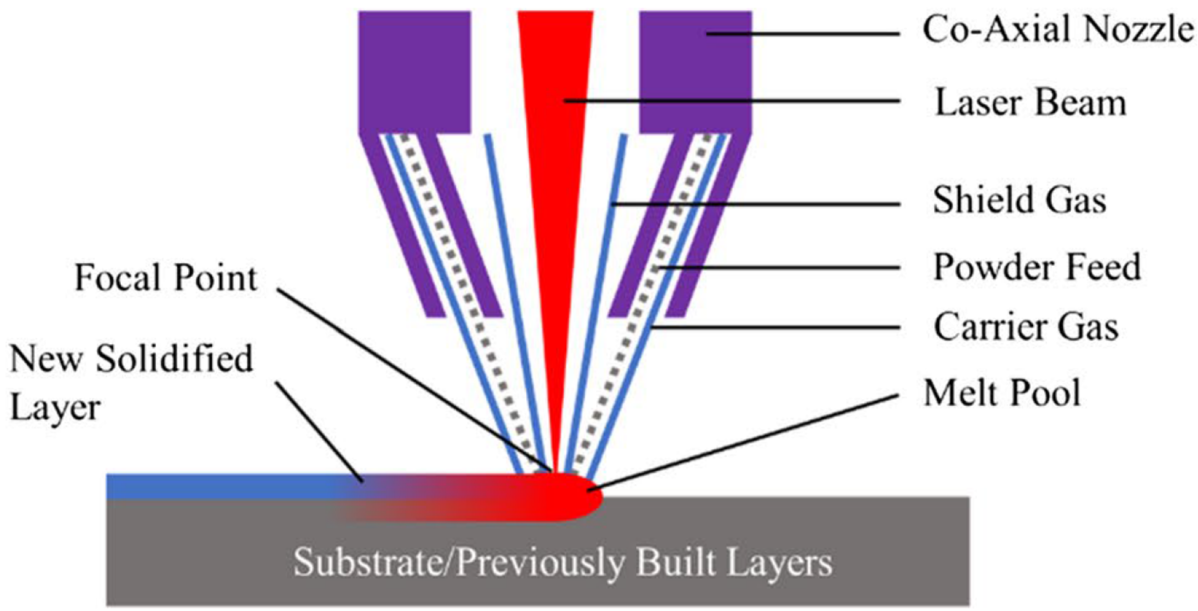

Figure 2.1: Deposition head's configuration showing the flow of the powder, shield gas, and carrier gas [27].

- **Functionally graded materials:** In certain applications, it is necessary for a part to have a smooth transition between different materials from one end to the other to have unique mechanical and metallurgical properties. With DED technology, parts are produced layer by layer, allowing for a gradual transition in feedstock material and the printing of parts with unique material properties [34]

- **Prototyping:** As DED processes build parts layer by layer from CAD models; therefore, it is enabling designers and engineers to create various metallic parts with different geometries for prototyping with a single setup. It will help to expedite the testing and design process [29]

- **Art and Architecture:** The DED process can be used to create metallic sculptures and architectural features with complex geometries and unique material combinations

- **Coating:** The DED process can be used to apply coatings of different materials over components. It will increase the corrosion resistance, wear resistance, etc. of the part and increase their life span [31]

Figure 2.2 shows the application of laser-based DED in manufacturing of complex parts, coating, and printing functionally graded materials.

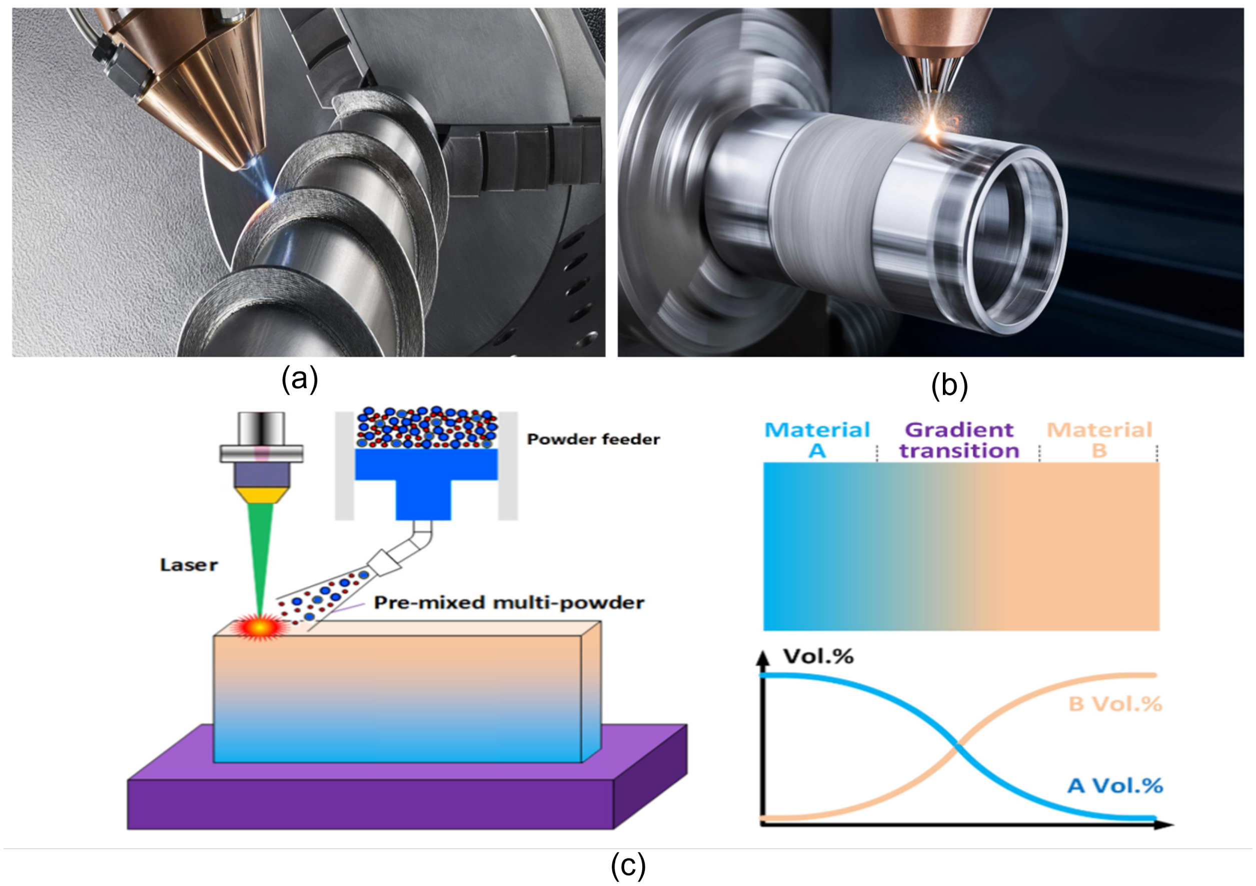

Figure 2.2: Applications of DED process in repair, manufacturing of complex part, and coating (a, b) [44], and manufacturing functionally graded materials (c) [20].

2.3 Powder DED Defects and Challenges

Despite the demonstrated advantages in industry, the DED process still faces challenges in producing high-quality parts that can be used in critical sectors, such as engine blades in aerospace. The quality of the final part depends on several factors, including (i) the built environment temperature; (ii) the interaction between the energy beam and material; (iii) deposition parameters (like laser power, scan speed, flow rate, scanning strategy, hatch spacing); and (iv) the feedstock material and its properties. Variations in the inputs of the DED process may result in defects such as:

- **Porosity:** During the DED process, the carrier gas or shield gas may be entrapped in the melt pool and result in pores in the printed layer. This defect lowers the strength and fatigue life of the parts [18]
- **Cracks:** The high thermal gradient between the melt pool and the solidified material in DED can cause stress to build up in the part, leading to the formation of cracks during the process.

These cracks can negatively impact the quality and fatigue life of the parts, reducing their overall performance [13]

- **Incomplete fusion:** During the DED process, if the input energy is insufficient to fully melt the powders in the melt pool, some powders may remain unmelted. This can result in poor adhesion between the layers and can degrade the mechanical properties of the final part [13]
- **Undesired residual stress:** Due to the rapid cooling and solidification during DED, parts can have residual stress that may lead to cracks and deformation [26]
- **Non-uniform layer thickness:** Due to variations in the main process parameters, such as power, flow rate, and scan speed, the deposition rate may vary and it can negatively affect the dimensional accuracy of the final product [54]
- **Poor surface finish:** Due to sintering of the remaining metal powder over the printed clad, surface quality will degrade; consequently, it can lower the quality of the final part by affecting its surface smoothness and texture [11]

Figure 2.3 shows formation of pores and cracks in the DED process.

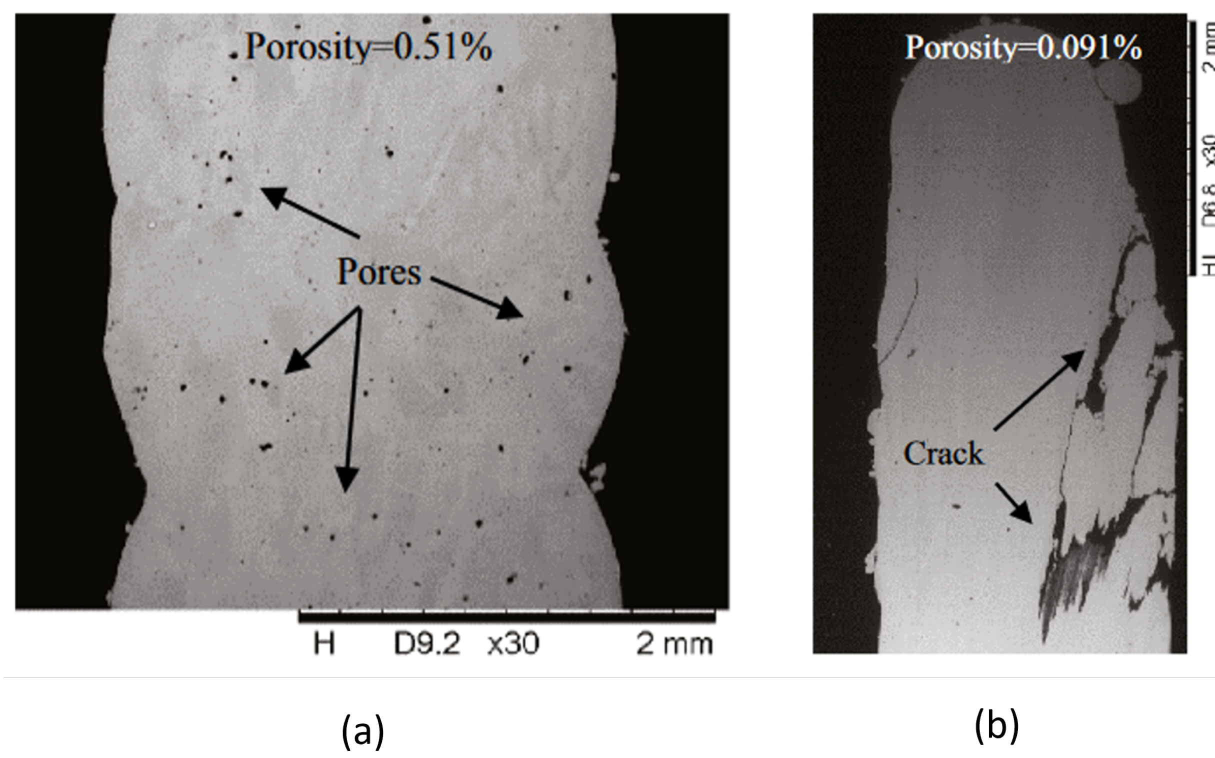

Figure 2.3: Defects in the DED process; formation of pores (a), and cracks (b) [6].

2.4 Post-Process Characterization and Process Monitoring

Post-process characterization and in-situ/online monitoring are two approaches for assessing the quality of parts and addressing the defects in the process. This section reviews the state of art on post-process characterization and in-situ/online monitoring.

2.4.1 Post-Process Characterization

Post-process characterization is essential for ensuring that 3D printed parts meet the desired specifications and quality standards, particularly in critical sectors such as aerospace and medical devices. To assess the quality of the parts, optical microscopy and Scanning Electron Microscopy (SEM) are commonly used to examine the geometry and microstructure of the deposited clads. X-Ray Diffraction (XRD) is a non-destructive technique commonly used to analyze the crystal structure and phase composition of the deposited material. It works by bombarding the material with X-rays and measuring the diffraction pattern, which can reveal information about the atomic arrangement and crystallographic orientation of the material. Dinda et al. [8] investigated the microstructure of the Al-Si thin walls using XRD. Their investigation shows the variations in the morphology and length scale of the microstructures at different locations of the thin wall resulting from different thermal histories at various locations. Energy-Dispersive X-Ray Spectroscopy (EDS) is a technique used to obtain the elemental composition of parts, including functionally graded material parts. It works by detecting and analyzing the X-rays emitted from a sample when it is bombarded by an electron beam. Yan et al. [49] used the DED process to manufacture functionally graded material parts by joining titanium aluminide Ti-48Al-2Cr-2Nb and commercially pure titanium with an innovative transition path. The EDS analysis over the part revealed the final composition was very close to the design composition. In the macro scale, the mechanical properties of the deposited material, such as hardness and tensile strength, etc., are measured to evaluate the performance of the parts[35, 49]. These tests help ensure that the part meets the desired specifications and quality standards in different sectors.

Post-process characterization methods can significantly improve quality control and assess the quality of the parts with high certainty and low relative error compared to in-situ monitoring. However, post-processing methods are often complex and expensive, and they cannot be used during the deposition process to immediately modify the process conditions if defects occur during the DED process resulting in the waste of energy and materials.

2.4.2 In-situ/Online Monitoring

In contrast to post-process characterization, in-situ/online monitoring is performed while the part is being printed, and in case of an error, the process can be stopped or modified to repair the defect.

It will result in less waste of energy and material and improves the efficiency of the process. During the DED process, the melt pool provides valuable information about the process. IR cameras and CCD/CMOS cameras are commonly used to capture the morphology of the melt pool, and pyrometers are used to measure the temperature of it in real-time. Song et al. [38] utilized three high-speed CCD cameras in a triangulation setup, along with a two-color pyrometer, to monitor and control the temperature of the melt pool and the building height during the DED process. Lijun et al. [39] utilized a feedback control system based on the melt pool temperature to stabilize the DED process, using a two-wavelength pyrometer.

Literature also focuses on the melt pool's morphological features, like size, length, area, etc. Schwerdtfeger et al. [33] investigated the possibility of in-situ anomaly detection by taking IR images of parts during the fabrication process and comparing them to metallographic images. They found a correlation between the patterns visible in IR images and metallographic images. Khanzadeh et al. [18, 19] utilized IR images of the melt pool and they were labeled as either pore or normal by X-ray tomography of the printed part. A supervised ML model was trained over the data to classify normal and defective melt pools during the process with high accuracy.

During online monitoring, visual sensors and pyrometers can only observe the surface of the melt pool, which limits their ability to accurately infer what is happening inside the melt pool. This can lead to uncertainties in decision-making. Additionally, the deposition process is a fast multi-physics phenomenon, which increases the signal-to-noise ratio in the data and decreases the certainty of the results.

2.5 Process Window of Powder DED

While subtractive manufacturing has established standards and highly formalized processes, DED is still an immature process with room for improvement. To ensure acceptable part quality with minimal defects, a process window must be identified for each DED setup, operating condition, and material. Abioye et al. [1] optimized the process parameters for the wire deposition of Inconel 628 and evaluated the quality of the clad based on criteria such as dilution ratio, good surface finish, and contact angle of less than 80° degrees. Jhavar et al. [16] determined the best process parameter for the wire deposition in μ-PTA process of AISI P20 tool steel by measuring the width and height of the cross-section of the tracks, and determining the quality of the track through visual examination. In another study, Bax et al. [5] systematically investigated the correlation between process parameters such as power, scan speed, flow rate, and the quality of clads for laser deposition of Inconel 718 using powder feedstock. Forend et al. [10] claimed that within the optimized process parameters range, it is possible to control the geometric shape, dilution, and aspect ratio of the deposited layers in a systematic way. They determined the process parameter window for the wire cladding of aluminum alloys using the DED process based on the surface quality of the clads, their cross-section geometry, and possible defects within them. Sun et al. [41] investigated the correlation between process parameters and the height, width, and dilution of layers in the powder deposition of Ti-6Al-4V. They found that the depth of the melt pool is highly correlated with scan speed in the process.

There have been numerous studies on identifying the process parameter window of the DED process for different setups and materials. Choosing the optimal process parameters can significantly minimize geometric errors, porosity, lack of fusion, and other defects that can impact the final quality of the printed parts; however, finding the proper process parameter requires sample preparation, iterations over different parameters, and inspections; but when selected, it would ensure printing parts with better quality.

2.6 Modeling and Control of Melt Pool Temperature

The temperature of the melt pool is a critical factor that influences the microstructural and mechanical properties of clads during the DED process. The temperature distribution is determined by the multi-scale thermal aspects of the process and is influenced by factors such as material properties, processing parameters, dwell time, scanning pattern, and so on. Understanding and controlling the temperature distribution in the melt pool is essential for achieving the desired properties in the final product[5, 35].

At the macro-scale, non-uniform temperature distribution can result in thermal-induced residual stress, distortion, uneven deposition, and cracks in the final part [50]. At the micro-scale, the uniform temperature distribution within the melt pool can improve the resulting microstructure of the part [52]. Thus, controlling the temperature distribution across scales is essential for achieving high-quality parts with desirable properties. Research has demonstrated the critical role of melt pool temperature in determining the quality of the final part. As a result, there have been many studies focused on controlling the temperature during the DED process to achieve desirable properties and ensure high-quality parts. Tang et al. [42] developed a controller for the melt pool based on an empirical formula that governs the melt pool temperature. They argued that process models available in the literature [9, 14] are too complex for online temperature control. Gibson et al. [12] measured the top-view size of the melt pool and designed a controller to keep the melt pool at the same size during deposition by adjusting the power. Smoqi et al. [37] developed a closed-loop control system to maintain a consistent temperature during the DED process. When the temperature deviates from the reference temperature, the system lowers or increases the power to the laser to maintain a constant temperature in the melt pool. Their results show improvement in the volume percentage of porosity and more consistent homogeneous dendritic microstructure. The majority of the approaches used in the control of the melt pool used a simplified version of the modeling for the melt pool or use real-time data of the melt pool from the experimental measurement during the deposition process.

Because modeling the melt pool's temperature and morphology is challenging, data-driven approaches can be effective for predicting the temperature based on the history of the melt pool. By training models on past data, these models can learn patterns and relationships in the data that can be used to predict future temperature behavior, without relying on detailed physical models of the DED process. Zhang et al. [53] utilized data-driven approaches to forecast temperature during the DED process. Time series analysis models such as LSTM were used to make predictions about future temperatures. Forecasting temperature in advance can be advantageous as it can provide early feedback to the controller for adjusting power, thereby compensating for process latency. The model used by Zhang et al. can only obtain the general trend of the temperature. On the other hand, this thesis focuses on training a data-driven model that can achieve a more accurate prediction of the temperature which can later be used for designing a controller.

Chapter 3

System Integration and DED Experiments

This chapter discusses the integration of the laser-based DED setup developed in our lab. The functionality of each of the components used in the DED machine is described. In addition, the sensors that are used in the machine, including an IR camera and a pyrometer, and how they are integrated into the system to measure the temperature and geometry of the melt pool are explained. Next, the software used to control the laser setup and the sensors, as well as the calibration procedures used to ensure accurate temperature measurements are discussed. Finally, the chapter ends with the results and discussions over the printed thin wall with the setup.

3.1 Integration of the DED System

The integration of the DED system includes establishing the connection of the hardware system and the development of the setup control software. The hardware consists of four main components: a motion stage, laser generator, deposition head, and powder feeder. This section provides some information about each component, including its functionality and mechanism of operation.

Motion Stage

In 3D printing, parts are fabricated layer by layer, hence a motion stage with at least 3 degrees of freedom is required. The motions in X and Y axes are utilized for printing in each layer, while the Z-axis motion is used for incrementing the deposition head after printing each layer. The ATS machine, which is a product of Dover Motion, is used as the motion stage for laser cladding. This machine is surrounded by opaque walls to block radiation from the laser and enable safe operation during the laser cladding process. The controller of the machine is using an open-source code written in MATLAB. The motion commands from the MATLAB script are interpreted into binary commands in the dSPACE and sent to the motion stage. The motion stage and its controller are shown in figure 3.1.

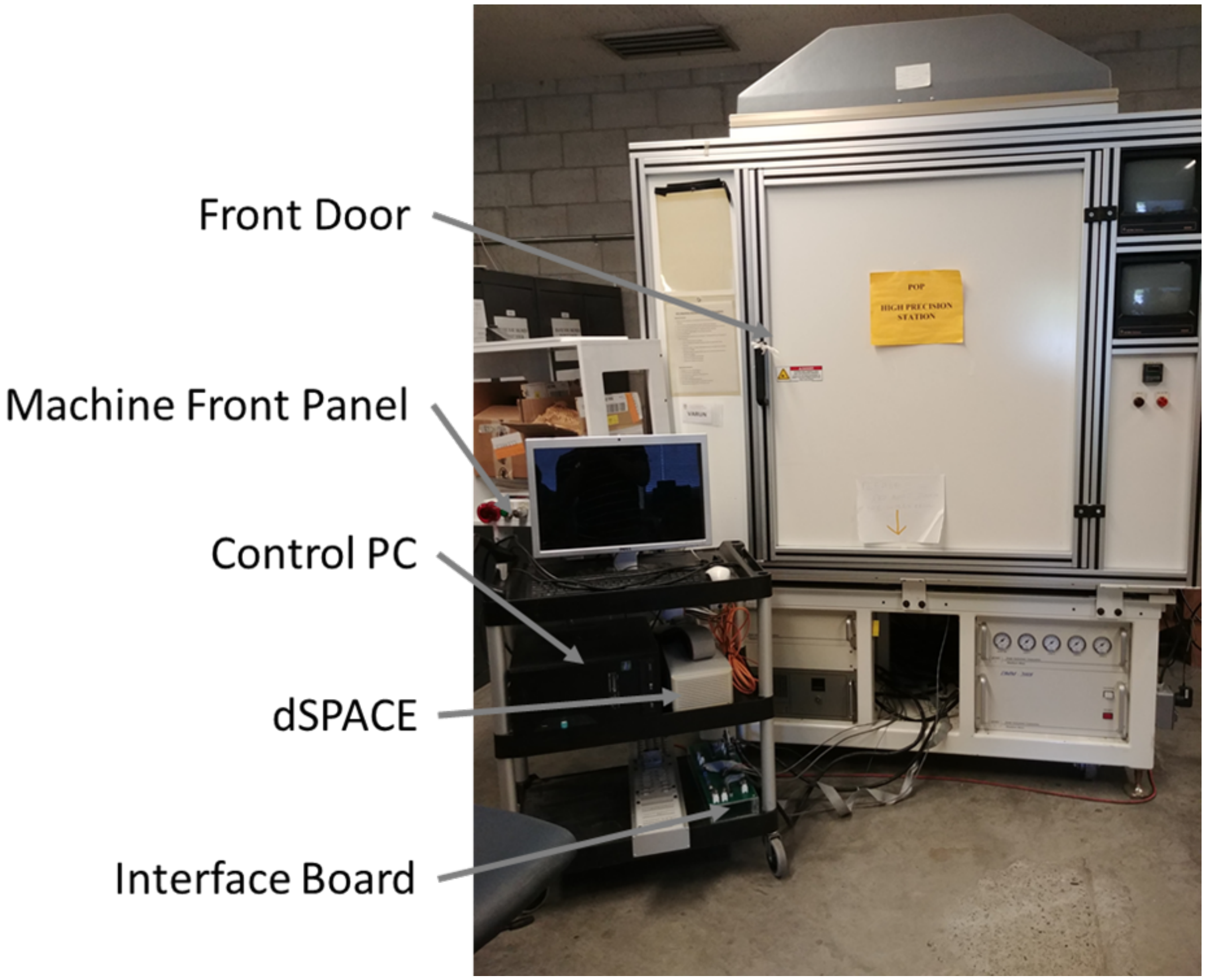

Figure 3.1: The 3-axis motion stage and its controller.

Laser Generator

To melt the metal powder during DED operation, the IPG YLR series fiber laser with a nominal power of 500 W and wavelength of 1070 nm are being used. The laser delivered to the surface has a Gaussian distribution. Also, it can generate a laser in continuous and pulsed modes.

Powder Feeder

The powder feeder is responsible for delivering the metal powder from the powder storage to the deposition head. The powder is carried by Argon gas, which also acts as the shield gas during the process. During the powder deposition process, metal powder is fed from the powder storage onto a rotating disc. The carrier gas, which is Argon, picks up the powder from the rotary disc by suction and delivers it to the deposition head. The flow rate of powder to the deposition head is determined by the rotating speed of the powder feeder's disc in RPM.

The relationship between the flow rate and the RPM of the rotating disc must be experimentally determined for each setup. To determine the flow rate, the shield gas was turned off and a plastic cup was placed under the deposition head nozzle to store the powder. The weight of the powder was measured for each RPM. The results and the fitted line are shown in figure 3.2. Eq 3.1 shows the relation between the RPM and the flow rate in grams.

$$flow\, rate = 5.151 \times RPM - 0.364 \tag{3.1}$$

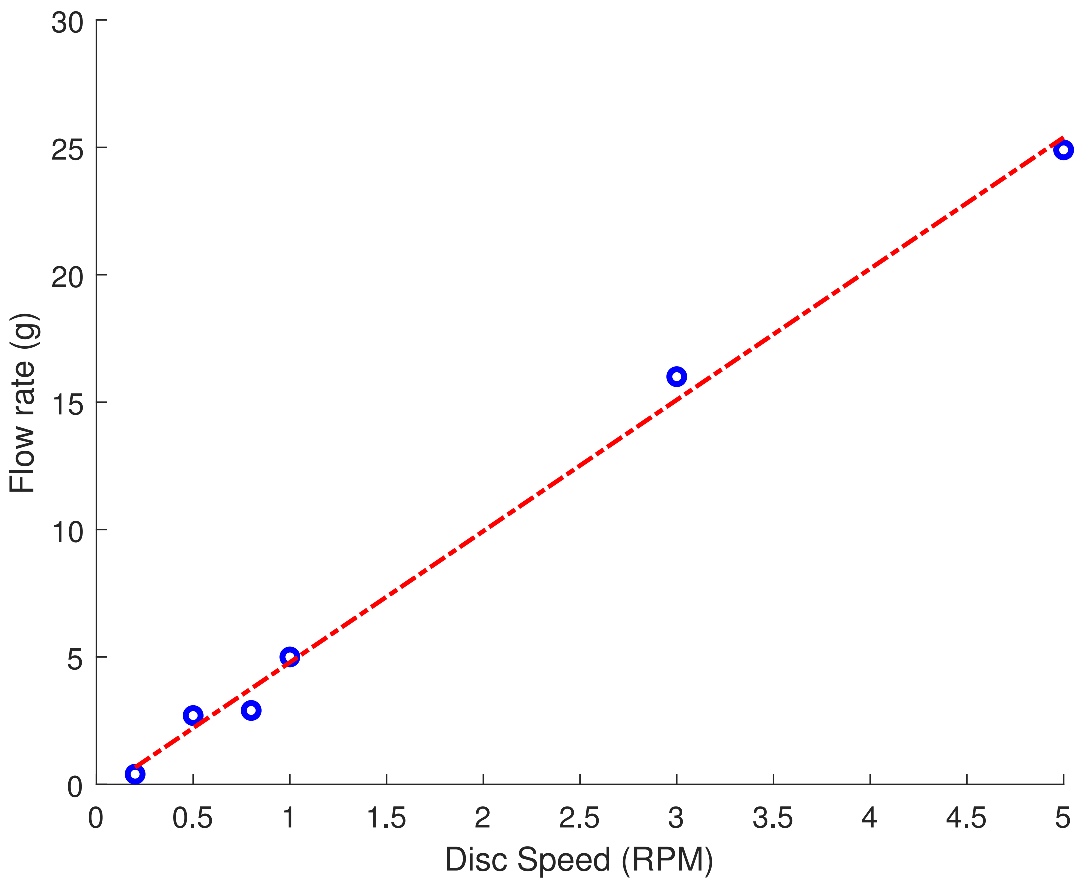

Figure 3.2: Change of mass flow (g) with respect to RPM in the powder feeder.

The powder feeder also delivers the Argon as the shielding gas to the deposition head. The shield gas is responsible for

- protecting the melt pool from oxidation
- protecting the deposition head optics from the metal powder

Deposition Head

The deposition head is one of the major components of the DED process. It is responsible for focusing the laser beam through its optics and co-axially delivering the metal powders and laser to the melt pool. An adaption plate was designed to integrate the deposition in the 3-axis machine. Figure 3.3 shows the deposition head installed on the motion stage.

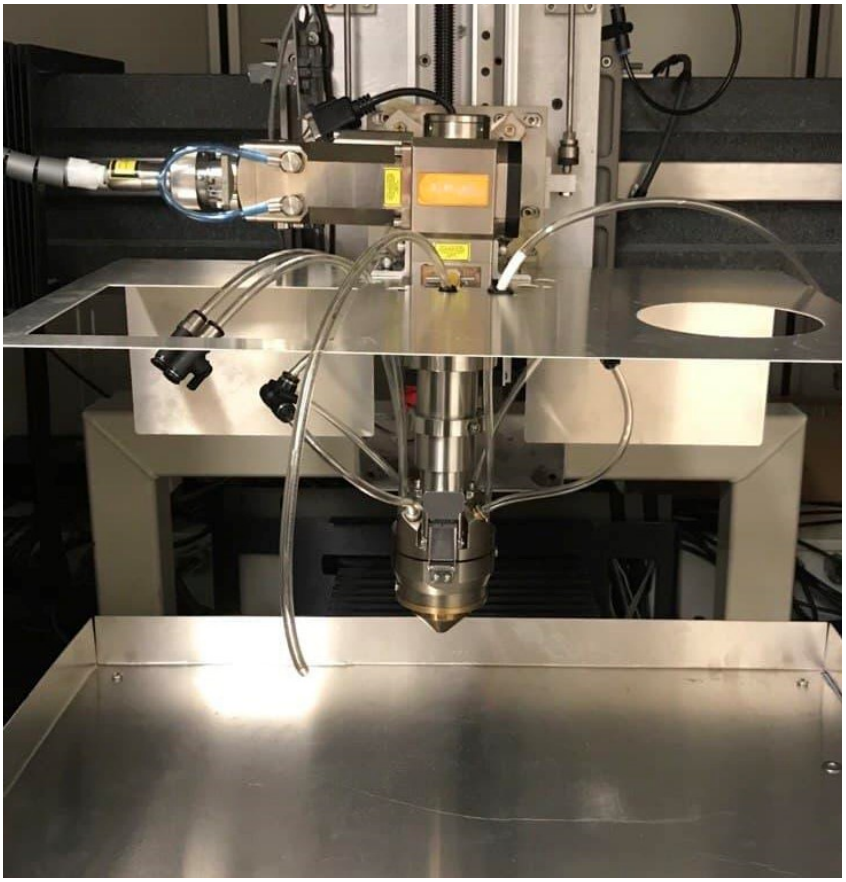

Figure 3.3: The deposition head of the DED machine.

3.2 Sensors

The main process parameters, i.e., laser power, scan speed, and flow rate, in the DED process directly affect the melt pool's morphology and temperature during the deposition. To obtain information about the temperature and morphology of the melt pool, a pyrometer, and an IR camera are installed, respectively. This section provides a brief background on infrared measurement technology and the sensors used in the setup.

3.2.1 Infrared Measurement

Michalski et al. [25] explain that when a heat flux Φ reaches the surface of a body, heat divides into 3 portions. A portion of it is being absorbed by the body, Φ_α; some portion is reflected. Φ_ρ; and the last portion is transmitted through the body, Φ_τ. Based on this observation, 3 physical properties can be defined: absorptivity $\alpha = \Phi_\alpha \backslash \Phi$, reflectivity $\rho = \Phi_\rho \backslash \Phi$, and transmissivity $\tau = \Phi_\tau \backslash \Phi$. Based on the principle of energy conservation, equation 3.2

$$\alpha + \rho + \tau = 1 \tag{3.2}$$

Based on equation 3.2, when $\alpha = 1$, $\rho = 0$, and $\tau = 0$, the body is defined as a black body and it absorbs and emits all the radiation. If $\alpha = 0$, $\rho = 1$, and $\tau = 0$, the body is defined as a white body and it reflects all the radiation. Lastly, when $\alpha = 0$, $\rho = 0$, and $\tau = 1$, the body is defined as a transparent body, and all the radiation is completely transmitted through it. These properties depend on the object's material, its surface, and temperature of it, and the radiation wavelength (λ) [25]. The basic idea in pyrometry is based on emissivity that is the ratio of the energy radiated from a material's surface to that radiated from a perfect emitter, a black body, at the same temperature and wavelength and under the same viewing conditions. Emissivity is a dimensionless number between 0 (for a perfect reflector) and 1 (for a perfect emitter). The emissivity of a surface depends not only on the material but also on the nature of the surface. For example, a clean and polished metal surface will have a low emissivity, whereas a roughened and oxidized metal surface will have a high emissivity. The emissivity also depends on the temperature of the surface as well as wavelength and angle.

One of the main advantages of using pyrometry to measure temperature is its capability for non-contact measurement. This provides the freedom to monitor hard-to-access surfaces and features, regardless of their location and orientation, while minimizing potential damage to sensors. One obstacle to using pyrometers and IR cameras is their relatively higher cost compared to thermocouples. Another limitation of pyrometry is the difficulty in calibrating these devices. The working principle of pyrometers and IR cameras is based on the emitted radiation of the body compared to the black body, and the accuracy of the temperature reading depends on the emissivity of the monitored object. However, in the DED process, the emissivity of the melt pool continuously varies due to its dynamic nature, making it relatively difficult to measure and achieve accurate readings. Considering all the benefits and challenges, pyrometers and IR cameras are the dominant techniques for monitoring temperature compared to thermocouples, due to their non-contact measurement features.

3.2.2 2-Wavelength Pyrometer

Pyrometers are used to measure temperature without contact, based on the emissivity and radiation from the object. However, a challenge in using pyrometers is emissivity-based measurement. To overcome this limitation, 2-wavelength pyrometers are used. 2-wavelength pyrometers utilize two distinct wavelengths to measure the hottest temperature in their field of view and read 2 different temperatures. As the phase difference between the 2 wavelengths is known, the pyrometer calibrates the temperature reading based on the wavelength values and the captured temperature values. Table 3.1 lists some specifications of the 2-wavelength pyrometer used in the setup, which is shown in figure 3.4.

Table 3.1: Specifications of the pyrometer

Model	CTRM-2H1SF100-C3
Temperature Ranges	550 to 3000°C
Focal distance	$>$ 300 mm
System accuracy	$\pm$ (0.5 % $T_{\text{of reading}}$ + 2°C)
Temperature resolution ($>$ 900°C)	0.1°C
Response time	1 ms

Figure 3.4: 2-wavelength pyrometer used for measuring melt pool temperature.

3.2.3 IR Camera

The morphology of the melt pool contains useful information, such as stability, shape, and temperature distribution. However, one of the main challenges in using an IR camera is the reliability of temperature readings. IR cameras use single-wavelength detectors to obtain radiation data, and temperature readings heavily rely on emissivity. In the melt pool, multi-physics phenomena, such as melting and solidification, occur, and the melt pool is also surrounded by an extreme amount of light and smoke that can hinder infrared detectors from obtaining information. Therefore, the IR camera is used to provide information about the morphology of the melt pool, not the melt pool temperature in the setup. Table 3.2 shows some specifications of the IR camera, which is shown in Figure 3.5.

Figure 3.5: FLIR IR camera used for getting the shape of the melt pool.

Table 3.2: Specifications of the IR camera

Model	FLIR A6750
Image resolution	640 $\times$ 512
Temperature range without filter	up to 100°C
Temperature range with filter ND1	45 °C to 600°C
Temperature range with filter ND2	250 °C to 2000°C
Data acquisition frequency	up to 120 Hz

3.3 Software Development for the Setup

In the DED setup, the following components have their own software and data acquisition system:

- Laser generator
- IR camera
- Pyrometer

To control the process, the laser power needs to be adjusted based on the feedback received from the sensors. However, when each component uses its own software system, their work is mutually exclusive, making connection difficult between devices. To overcome this obstacle, open-source software has been developed to integrate the control of all components and enable coordinated control of the process.

3.3.1 Software's Functionality

The software has been written in Python, utilizing the PyQt5 library to develop a Graphical User Interface (GUI) that enables users to initialize and set power for the laser generator and retrieve data from the pyrometer and IR camera. The software stores the data captured by the IR camera and pyrometer in a database, using time as the primary key. To ensure smooth communication with multiple components, multi-thread software has been designed, allowing it to send and receive signals without freezing. The software is connected to the following components:

- Laser generator
- Pyrometer
- IR camera

Laser Generator

The laser generator is connected to the server via an Ethernet connection; the hardware inside the laser communicates through serial commands with the server. The manual for the laser generator provides a list of all the serial commands for the laser generator and their functionality. The designed Graphical User Interface (GUI) includes a section that is specifically for the laser, allowing users to send commands for turning on the laser generator, setting the power, and turning the guide beam on and off. The software also sends a command to retrieve information from the laser box, such as the delivered laser power and the temperature of the laser box.

IR Camera

The IR camera comes with commercial software that offers advanced processing and data acquisition capabilities. However, it does not have an accessible API that can be used to communicate with other software via HTTP commands. To obtain data from the IR camera, the Python code provided by the company is used. The code reads the data from the IR camera and does all the processing to convert it to temperature values. The provided code was integrated into the backend of the software to read the temperature data into the designed software. The data is plotted in real-time and stored in the database.

Pyrometer

The final component is the 2-wavelength pyrometer. The pyrometer is connected to the server via USB. There are some predefined serial commands by the manufacturer that can be used to access the pyrometer's data from the software. The software sends the serial command specified for reading the temperature and the pyrometer sends the temperature value in real-time as the response.

Temperature Calibration

After collecting data from both the IR camera and the pyrometer, the data from the pyrometer is used to calibrate temperature readings. As mentioned earlier, the temperature readings from the IR camera are heavily dependent on the emissivity of the object being measured. Therefore, they need to be calibrated by the data from the 2-wavelength pyrometer, which is not dependent on emissivity. To calibrate the temperature readings from the IR camera, the temperature measured by the 2-wavelength pyrometer is used to scale the maximum temperature reading of the IR camera and set the rest accordingly.

3.4 Printing a thin wall

Once the setup was integrated, a thin wall was printed to test the performance of the setup and gain further insights into the process. The specifications of the thin wall are listed in Table 3.3. Two thin walls, each including 20 and 40 layers, were printed using the bi-directional scanning pattern, shown in figure 3.6. Based on figure 3.7, although one of the thin walls has twice the number of layers compared to the other, their heights are not necessarily following the same ratio. This is because the deposition height may vary for the same process parameters in different layers during the printing process.

Both ends of the thin wall have a lower wall height compared to the middle section. When the bi-directional pattern is used for printing a thin wall, heat accumulates on both ends, causing the wall to slowly creep downwards before solidification. This downward creeping results in a lower height on both ends of the wall.

Table 3.3: Thin wall's parameters

Power	450 W
Scan speed	2 mm/s
Powder Flow rate	1 g/min
Scanning pattern	bi-directional

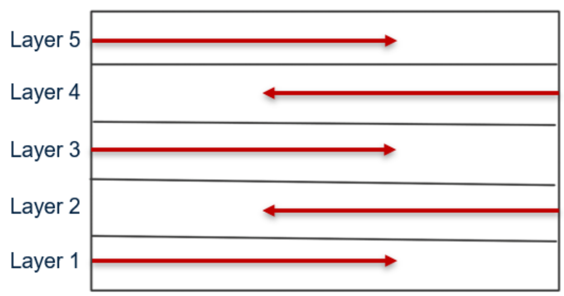

Figure 3.6: Schematic of the bi-directional printing pattern.

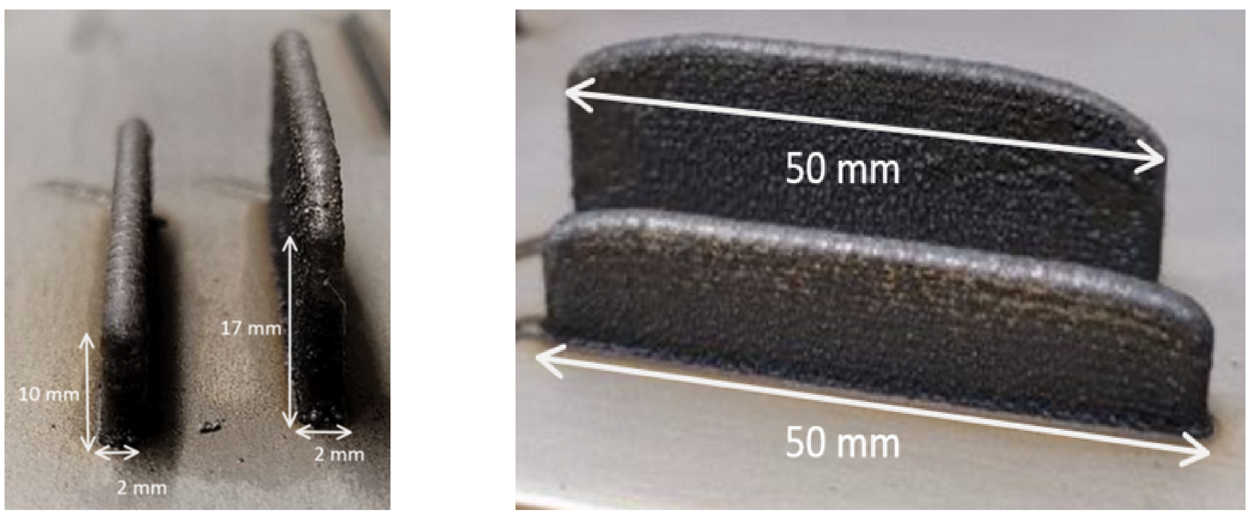

Figure 3.7: Thin wall with 20 and 40 layers.

3.5 Conclusions

In summary, this chapter illustrates the integration of the components and sensors into the 3-axis motion stage to make the DED setup. After integration, software and the GUI for the laser generator, 2-wavelength pyrometer, and IR camera were developed to facilitate the control of the laser based on the feedback of the sensors in future studies, also the software uses the temperature data from the 2-wavelength pyrometer to calibrate the measurement by the IR camera, which is highly dependent on the emissivity of the object. Finally, to test the performance of the DED setup, a thin wall with multiple layers was printed and the possible reasons for deformations on both ends of the thin wall were analyzed.

Chapter 4

Determining the Process Window

Metal 3D printing involves building parts layer by layer. To achieve satisfactory dimensional accuracy, good bonding, and improved surface finish, among other desired outcomes, it is important to study the process layer by layer to ensure the quality of the deposited layer before the addition of the next layer over it. Figure 4.1a shows a printed square with several layers, using parameters, including the power of 500 W, the flow rate of 4 g/min, the scan speed of 4 mm/s, and z-axis increment of 0.5 mm, that were taken from the literature [4]; but the final result is not satisfactory due to the high variation across process parameters of different DED machines; therefore those process parameters can't be used for the setup used in this thesis. In order to print high-quality parts using the DED process, it is necessary to carefully study and optimize the process parameters for the experimental setup to print a part like figure 4.1b, which has better quality compared to the other one. This square is printed with the power of 350 W, the flow rate of 2 g/min, the scan speed of 2 mm/s, and the z-axis increment of 0.3 mm, that are determined as the proper process parameter for this setup. This chapter focuses on the determination of the process parameters for the first layer, in order to achieve high-quality tracks with consistent and repeatable results.

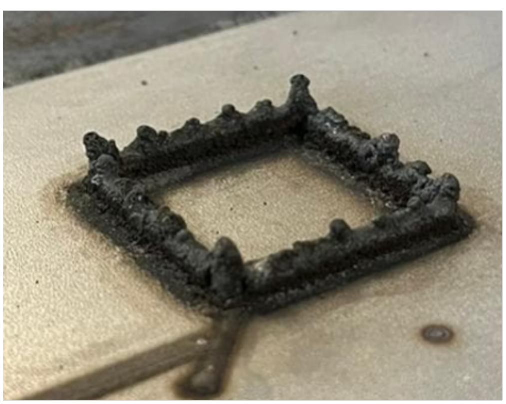

(a) Improper process parameters

(b) proper process parameters

Figure 4.1: Printed square with multiple layers using improper (power=500 W, scan speed=4 mm/s, flow rate=4 g/min, and z-axis increment=0.5 mm) (a) and proper (power=350 W, scan speed=2 mm/s, flow rate=2 g/min, and z-axis increment=0.3 mm) (b) parameters.

4.1 Materials of Powder and Substrate

A mild steel plate with a thickness of 7 mm is used as the substrate, and its composition can be found in Table 4.1. In order to improve laser absorptivity and ensure uniform deposition with good bonding of the clads to the substrate, the top surface of the metal plates was sanded to achieve a smooth and flattened surface. The plates were cleaned with water and soap to ensure that no grease remained on the surface. Figure 4.2 shows the clads that were deposited on an unprepared substrate; it resulted in clads without good bonding and a constant deposition rate. Stainless Steel (SS) 316 was used as the powder for the metal deposition process. The composition of the powder can be found in table 4.2, reported by the suppliers. The powder was produced through gas atomization, and additional specifications such as particle size, shape, density, etc. can be found in table 4.3.

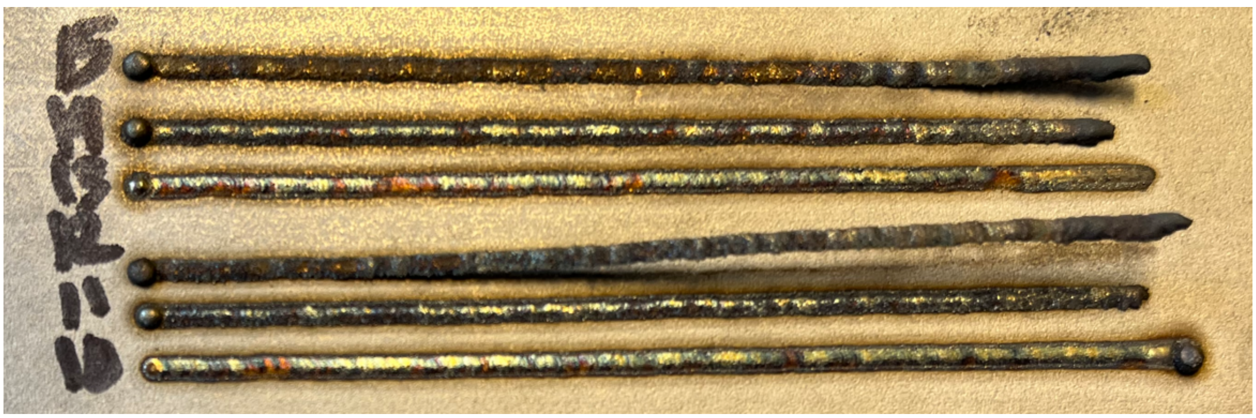

Figure 4.2: Depositing clads over the unprepared substrate resulting in nonuniform clads without good bonding to the substrate.

Table 4.1: Substrate's composition (mild steel)

Carbon	**Silicon**	**Manganese**	**Sulphur**	**Phosphorus**
0.16-0.18%	0.4% Max	0.7-0.9%	0.04% Max	0.04% Max

Table 4.2: Metal powder composition (SS 316)

Cr	**Ni**	**Mo**	**C**
16-18%	10-14%	2-3%	0.03%

Table 4.3: Metal powder specifications

Average powder size	25 μm
Powder shape	Spherical
Tap density	5 g/cm^3
Appearance	Gray

4.2 Experimental Plan

Although there are many possible combinations of process parameters in which the setup is capable of printing, only a few of these combinations are of sufficient quality to be used. Table 4.4 displays the range of output values for each component in the setup, which can result in a wide range of process parameters. As a result, it is crucial to identify a range for each of the process parameters, including power, scan speed, and flow rate, resulting in tracks with good quality, geometry, and bonding to the substrate; This certain range for the process parameters is known as the process window.

Table 4.4: Range of the outputs for each component

Parameters	**Range**
Laser power	0 to 500 W
Powder feeder	0 to 30 g/min
Motion speed	0 to 200 mm/s

4.2.1 Process Parameter Selection

To determine the appropriate process parameters for the experiment, preliminary experiments were conducted, and literature was studied to obtain an idea of the approximate range of process parameters. The selected range for printing a single clad is shown in Table 4.5. There are six parameters for power, five for flow rate, and five for motion speeds, which when combined, result in 150 clads with different process parameters, each with a track length of 7 cm.

Table 4.5: Selected values of power, flow rate and scan speed to conduct the experiment

Parameters	**Input parameter**
Laser power	250, 300, 350, 400, 450, 500 W
Powder flow rate	0.5, 1, 2, 3, 4 g/min
Scan speed	2, 4, 6, 8, 10 mm/s

4.3 Sample Preparation

After depositing the clads onto the substrate, samples were cut using a water jet to examine the cross-section of the sample. Figure 4.3 presents the cross-section of the samples. Based on this image, only a rough estimate of the clad height and width can be obtained. To improve measurement accuracy and gain more insight into the melt pool, samples need to be ground, polished, and etched. This section provides a detailed sample preparation procedure.

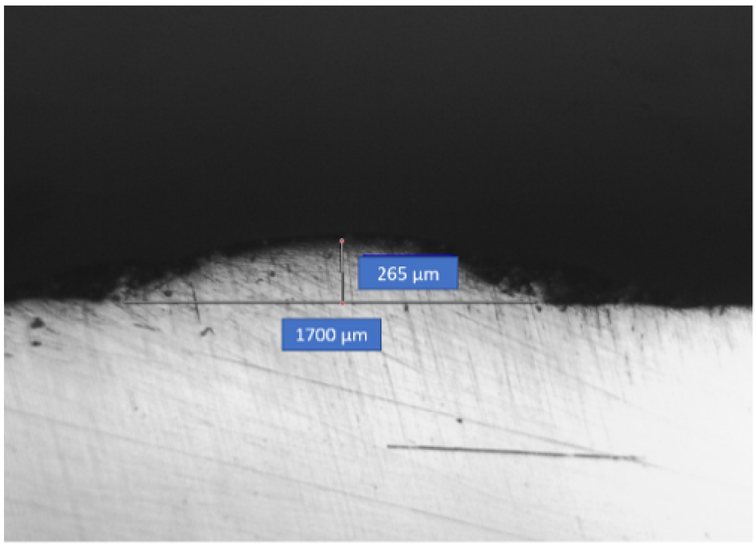

Figure 4.3: Unprepared cross section of the samples.

4.3.1 Grinding Step

To prepare the samples, a manual polishing wheel was used. Samples were mounted and ground with grinding papers of 400, 600, 800, and 1200 grits. After each step of grinding, the samples were analyzed under a microscope to ensure the quality of the grinding. Next, the sample was rotated by 90°, and the finer grinding paper was used for the next step of grinding.

4.3.2 Polishing Step

After grinding up to 1200 grits, the samples are polished using water-based diamond suspensions with the size of 6, 3, and 1 μm. Like grinding, after each polishing step, samples were analyzed under a microscope to ensure the quality of polishing and then rotated 90 degrees for the next polishing step with the finer diamond sizes.

4.3.3 Etching

Materials have different chemical compositions and properties, which results in different reactions to acids that have corrosive behavior. In this thesis, the substrate is made of mild steel and the powder is made of SS 316. During deposition, the final clad material is a combination of both mild steel and SS 316. As the etchant has different corrosion rates on the clad and the substrate, it will reveal the melt pool shape inside the substrate and further analysis of the depth of the melt pool and the quality of the clad can be done.

Determining the appropriate etchant and etching time is an iterative process. Firstly, it is necessary to identify the appropriate etchant that can effectively etch the surface. Then, an iterative approach is used to determine the best etching method and time that can reveal the melt pool shape inside the substrate without causing under-etching or over-etching of the surface.

In order to find the proper etchant for SS 316 and mild steel, literature [2, 37, 47, 51] was studied and the following etchants were selected for trials on the clads and the substrate in order to determine the best etchant.

- Adler's etchant (figure 4.4a)
- Villela's etchant (figure 4.4b)
- Nital 5% etchant(figure 4.4c)
- Marble's etchant (figure 4.4d)

Based on the results in figure 4.4, it can be observed that Adler's and Marble's etchants are not suitable because they cause burning of the parts. Nital 5% does not reveal the difference between the two materials. Lastly, Villela's etchant is much more effective than the rest. The composition of Villela's etchant is shown in table 4.6. After finding the proper etchant for the clads and the substrate, the suitable etching time and method need to be found iteratively to obtain a surface that is neither under nor over-etched.

Table 4.6: Villela's etchant composition in percentage

Picric Acid	**Hydrochloric acid**	**Ethanol**
1 %	10%	89%

Once a suitable etchant has been identified, it is necessary to perform iterations to determine the proper etching method and time. There are 2 common etching methods:

- Immersion (the result is shown in figure 4.5a)

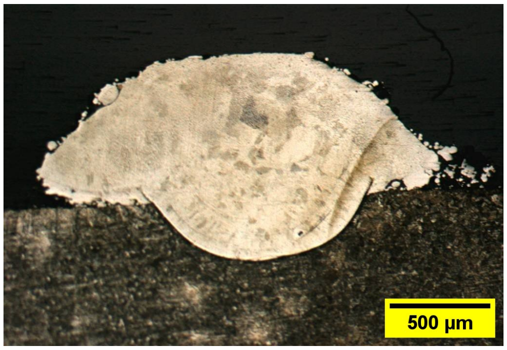

(a) Adler's etchant

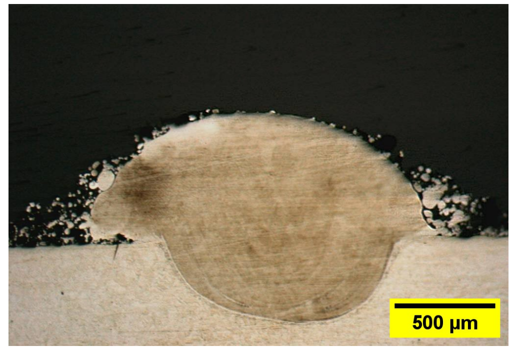

(b) Villela's etchant

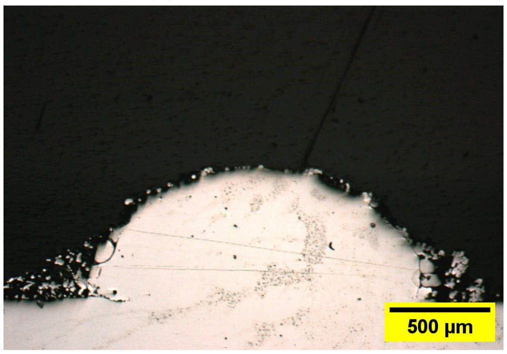

(c) Nital etchant

(d) Marble's etchant

Figure 4.4: Effect of different etchants over the clads and the substrate.

- Scrubbing (the result is shown in figure 4.5b)

In immersion, the part can be immersed fully in the etchant, or droplets are used to place the etchant's drops over the desired location. In the other method, a scrub, that was previously soaked into the etchant, is used to scrub and etch the surface. In scrubbing, there is the possibility of not applying force evenly over the surface or because of the motion of the scrub, a part of the surface can be more exposed to the etchant compare to the other locations; therefore, the immersion method produces better and more uniform results compared to scrubbing as shown figure 4.5.

After finding the best etchant and etching method, an iteration should be done on the etching time to find the proper timing. Based on the documentation for Vilella's etchant, an etching time of 1 to 5 minutes was suggested. After conducting several iterations, the etching time of 4 minutes is selected to produce the desired results.

4.4 Analysis on the Geometry of Clads

After printing 25 clads for each laser power (a combination of 5 flow rates and 5 scan speeds), it was noticed that among all the 5 speeds, only the scan speed of 2 mm/s provided enough time for

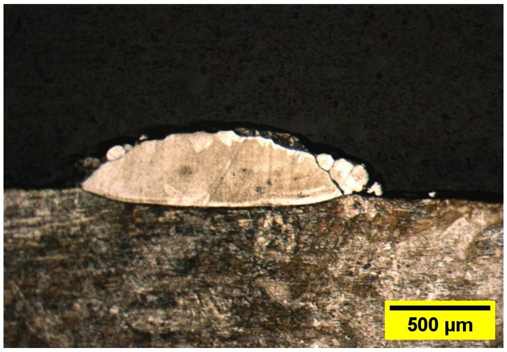

(a) Scrubbing method

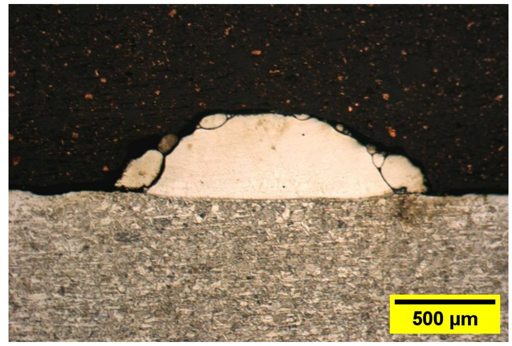

(b) Immersion method

Figure 4.5: Effect of scrubbing and immersion methods for apply the etchant over the surface.

the laser to melt the substrate and powder. It was observed that at higher scan speeds, a very small amount of powder was deposited, and there was minimal difference between the height of the deposited clads. For instance, varying the powder flow rate at scan speeds of more than 2 mm/s resulted in a very subtle change in the height of the deposited clad. The scan speed of 4 mm/s and 500 W power yield relatively good results compared to the rest of the powers in scan speed of 4 mm/s, but it was not considered in the results for the sake of consistency with the rest of the power's scan speed. Therefore, all the analyses are conducted for the scan speed of 2 mm/s, which includes 30 tracks.

4.4.1 Height Analysis over Clads

Maximizing the height of the clad is important as more height per clad results in faster printing and time and energy savings. However, there must be a trade-off between the height of the clads and their quality, i.e., good clad geometry and proper bonding to the substrate.

Height variation at different powers

During the DED process, the amount of metal powder supplied to the melt pool is typically greater than what is required, and not all of it can be captured by the melt pool. When the laser power is increased at a constant flow rate, it results in melting more metal powder on the fly and creation of a larger melt pool that together results in capturing more metal powder and more deposition rate. This leads to an increase in the clad's height for the same flow rate and higher laser powers. The maximum height of the clads with respect to the power is shown in figure 4.6; based on the figure, in some flow rates, the clad's height is higher in the power of 450 W compared to the power of 500 W. When the laser power increases from 450 to 500 W, a melt pool with a larger diameter is formed over the surface and results in clads that have a larger width and lowers height compared to the power of 450 W as shown in figure 4.7. This increase in the width of the clads also exists in the lower flow rate but because the flow rate is lower, it is not magnified like the higher ones.

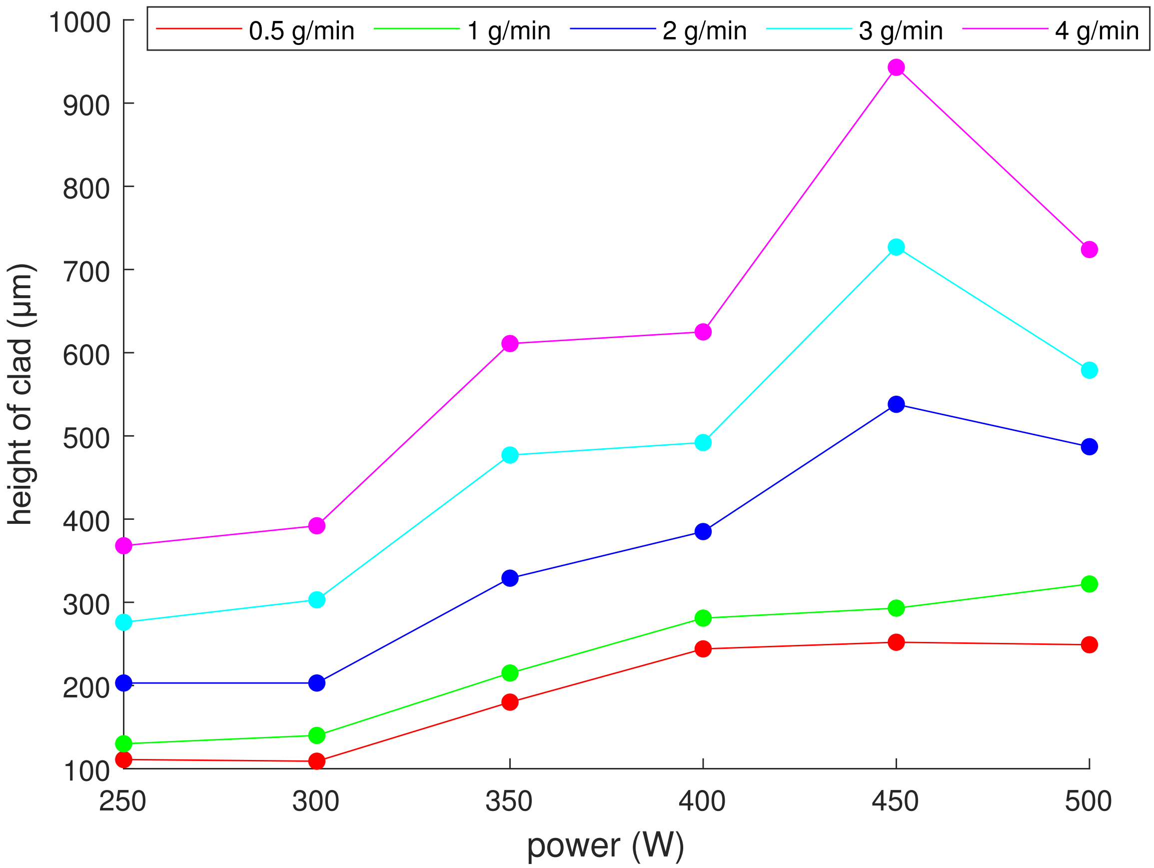

Figure 4.6: Height of the clads at different powers and constant flow rate.

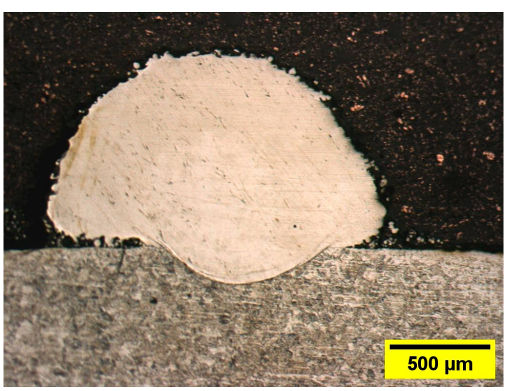

(a) Power 450 W

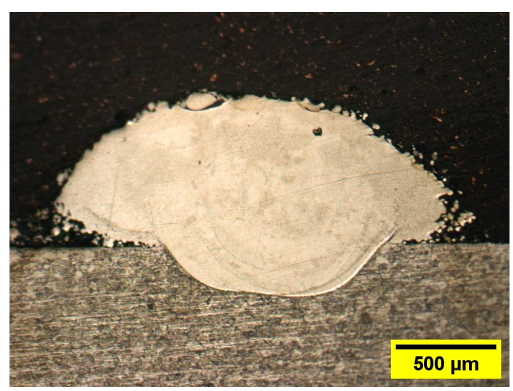

(b) Power 500 W

Figure 4.7: Variation in the height and width of the clads and melt pool in power 450 W (a) and power 500 W (b) in the flow rate of 4 g/min.

Height variation at different flow rates

The outlet size of the nozzle used in the DED process remains constant, so increasing the flow rate results in an increase in the area density of the powder being sent from the nozzle. Consequently, at the same power level, increasing the flow rate enhances the likelihood of melting more powder due to the increased area density, which ultimately results in an increase in clad heights. The maximum height of the clads is measured and the height variations at different flow rates and constant powers are shown in figure 4.8.

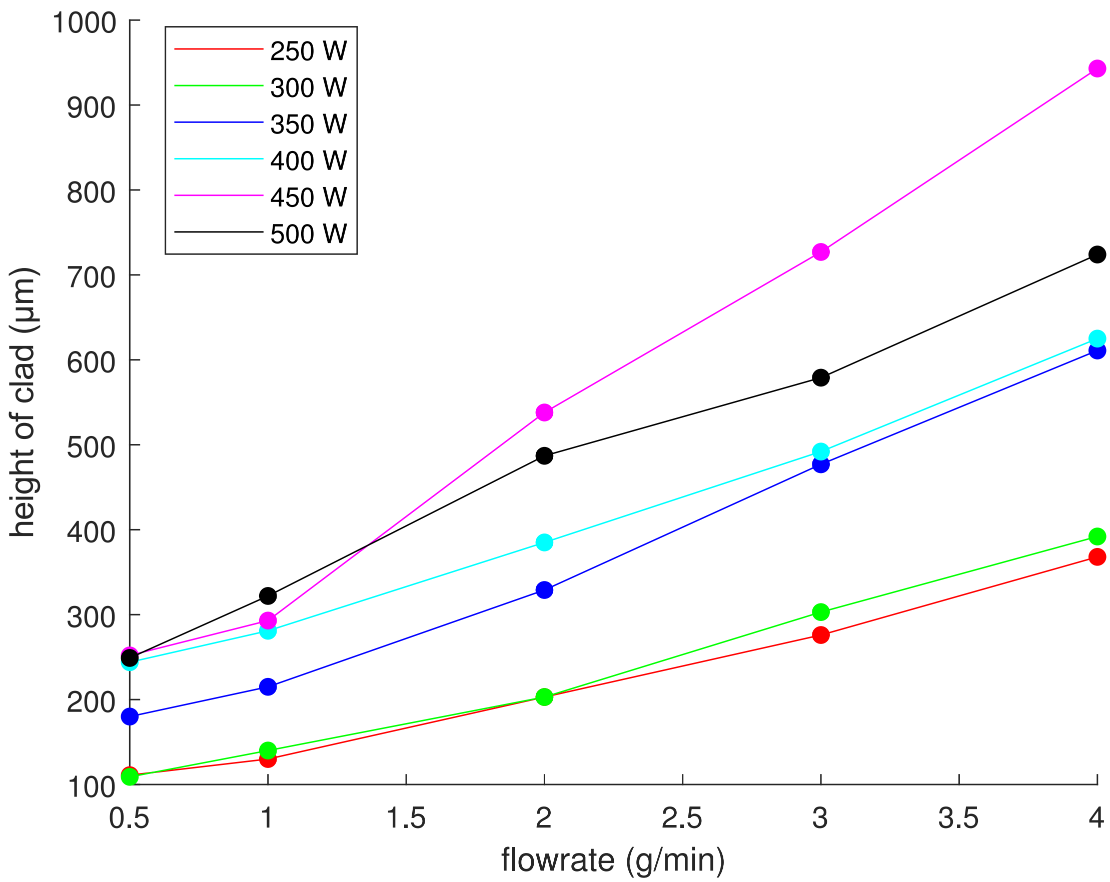

Figure 4.8: Height of the clads at different flow rates and constant power.

4.4.2 Melt Pool Depth Analysis over Clads

One of the challenges in metal 3D printing is the formation of pores in the DED process that will degrade the part quality and lower its fatigue life. The metal powder is carried to the melt pool with the Argon gas and there is the possibility of entrapment of the gas within the melt pool before solidification, resulting in the formation of pores. When the laser melts deeper in the previous layer and forms a larger melt pool, the possibility of entrapment of the gas and pore formation increases. Therefore, it is necessary to set the process parameters to minimize the depth of the melt pool while ensuring proper bonding to the substrate or the previous layer.

Melt pool depth variation at different powers

During the DED process, the laser emitted from the nozzle first encounters a cloud of metal powder and melts a portion of the powder on the fly. After penetrating the powder cloud, the laser gets to the substrate and forms a melt pool. The higher the power of the laser, the more energy reaches the substrate that results in a deeper melt pool on the substrate. The variation of the melt pool depth with respect to power at a constant flow rate is shown in figure 4.9. Based on the figure, with the increase of the laser power, a deeper melt pool is formed. Also, as the melting temperature of the mild steel, the substrate, is higher than the melting temperature of SS 316 by around 75°C, in the laser powers of 350 W and lower, the laser can't provide enough energy to fully create the melt pool inside the substrate and the depth of the melt pool remains around the same range, but for the powers larger than 350 W, the laser can provide sufficient power to melt the mild steel and the more increase in the power would result in deeper melt pool inside the substrate.

Melt pool depth variation at different flow rates

When the flow rate increases at the same laser power, the area density of the powder in front of the nozzle increases. This cloud of powder acts as a barrier for the laser to penetrate and reach the substrate, resulting in a decrease in the depth of the melt pool. Results are shown in figure 4.10. Based on the figure, with an increase in the flow rate, the depth of the melt pool decreases.

4.5 Dilution

One of the primary characteristics to evaluate the quality of a clad is its dilution, which determines whether the clad is properly bonded to the surface of the substrate while having a good deposition rate. The dilution is calculated by equation 4.1, where A1 and A2 are the area of the clad over and under the surface of the substrate, respectively, shown in figure 4.11. The areas are measured by counting the pixels of each section and scaling them based on the microscope's scale bar. Based on this approach, dilution for all the clad printed with the scan speed of 2 mm/s was computed.

$$\eta = \frac{A_2}{A_1 + A_2} \tag{4.1}$$

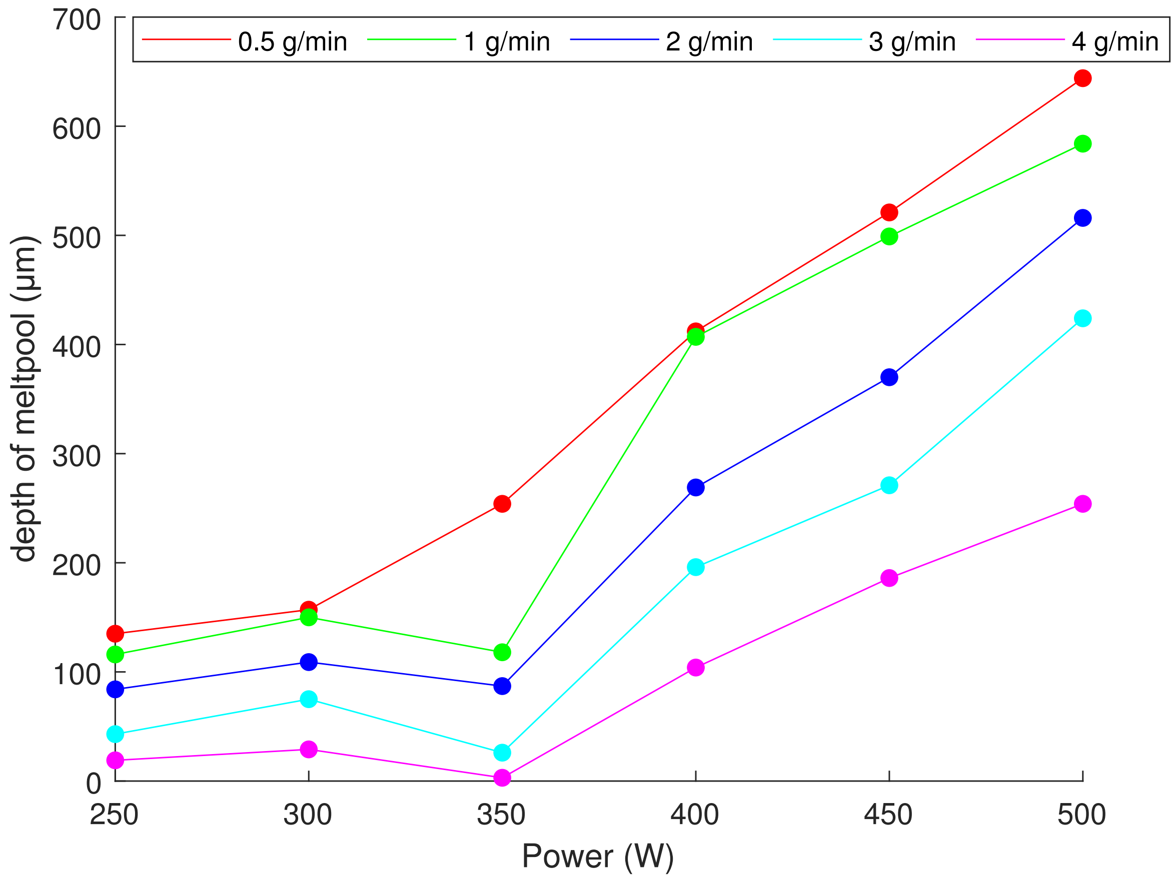

Figure 4.9: Depth of the melt pool at different powers and constant flow rate.

4.5.1 Variation of Dilution at Different Flow Rates and Constant Power

Figure 4.12 displays the relationship between dilution and flow rate at constant laser power levels. The figure indicates that increasing the flow rate results in a reduction in dilution. Increasing the flow rate results in an increase in the area density of the metal powder. With higher density in the powder cloud, more energy is absorbed by the cloud and more metal powder is melted; therefore, less energy is available to melt the substrate, and a decrease in the size of the melt pool in the substrate results in lower dilution values at higher flow rates.

4.5.2 Variation of Dilution at Different Powers and Constant Flow Rate

Based on figure 4.14, increasing the laser power results in an increase in dilution. The cloud of metal powder first absorbs the laser power and the laser melts the powder on the fly and the remaining power reaches the substrate and creates a melt pool. When the laser power is increased, the power reaching the substrate becomes proportionally larger, resulting in a larger melt pool under the

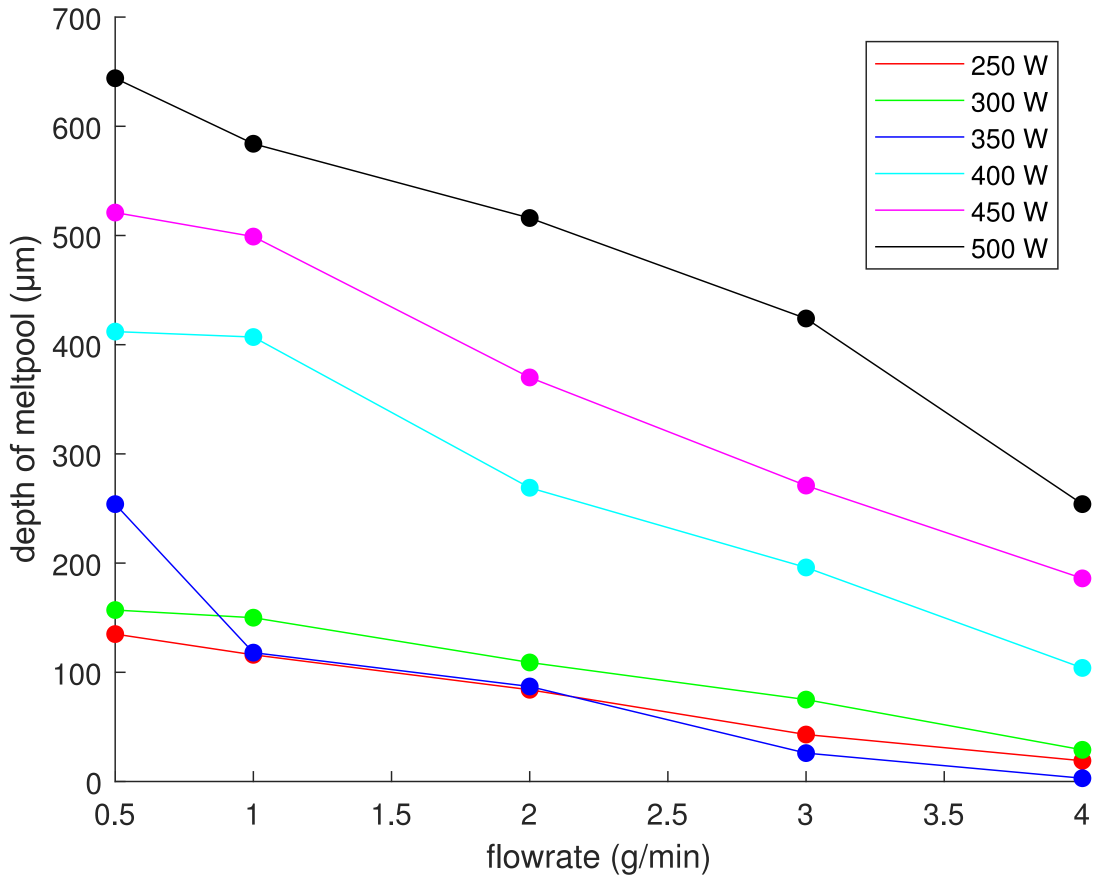

Figure 4.10: Depth of the melt pool at different flow rates and constant power.

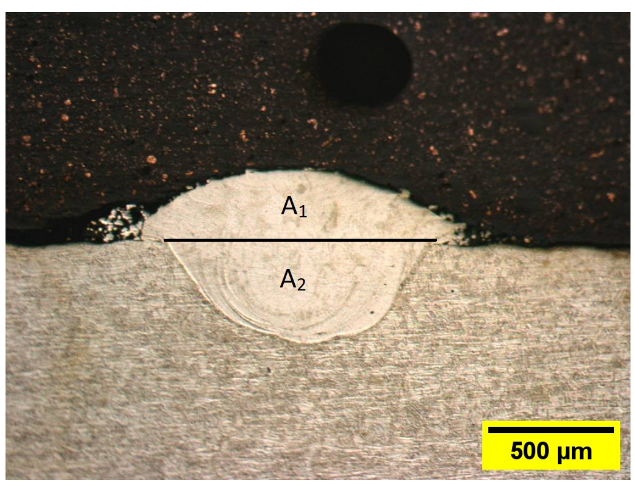

Figure 4.11: Areas used in calculation of dilution.

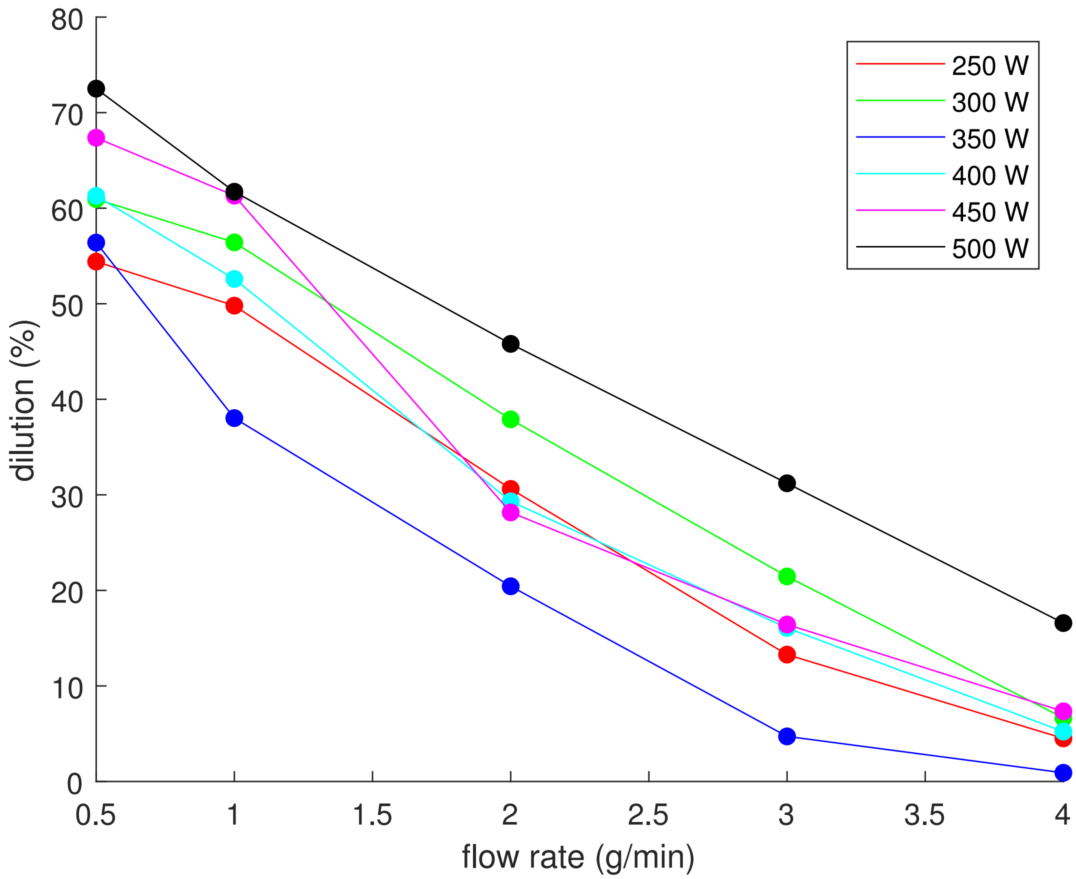

Figure 4.12: Variation of dilution at different flow rates and constant power.

surface of the substrate; consequently, the dilution increases. Based on figure 4.14, there is a local minimum in value of dilution in each flow rate at the laser power of 350 W. This local minimum is because of the physical properties of the metal powder and the substrate. Metal powder, SS 316, melts around 1375° C while mild steel has an average melt point around 1450° C that is higher than the powder's melt point. When the laser power goes beyond 350 W, it will provide more power for melting the substrate and will make a deeper melt pool, as shown in figure 4.13; consequently, results in an increase of dilution. For the laser powers below 350 W, laser power is not able to do the deposition as high as laser power of 350 W; therefore the clad's area on top of the surface is relatively smaller. In the power of 350 W, the laser power gets to an optimum point where it can melt more metal powder compared to powers below 350 W to deposit a clad with more height, and also it is not providing enough energy for the substrate to create a melt pool inside it. Therefore, it will result in a drop in the dilution value at the power of 350 W compared to the other powers, which is desirable.

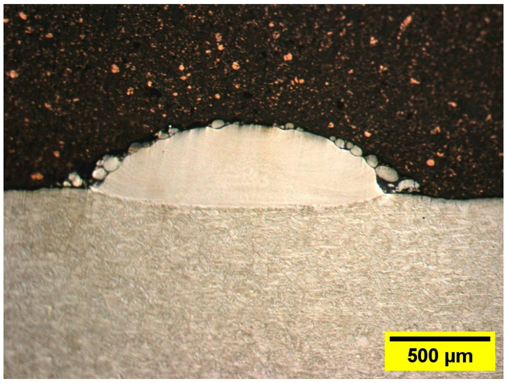

(a) Power 350 W

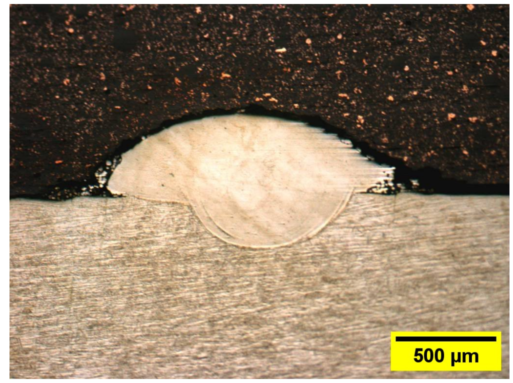

(b) Power 400 W

Figure 4.13: Change in the shape of the melt pool in laser powers of 350 and 400 W and same flow rates.

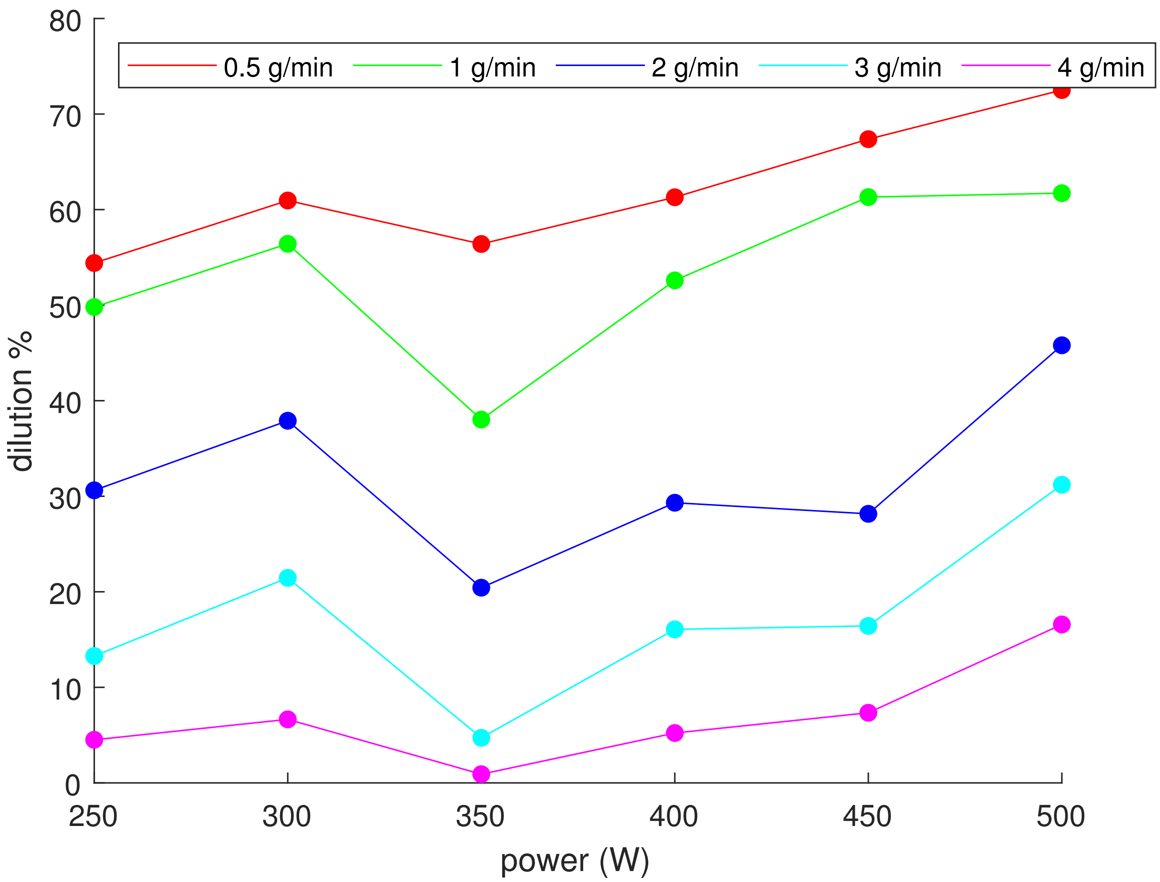

Figure 4.14: Variation of dilution at different powers and constant flow rate.

4.5.3 Variation of Dilution at Different Power Densities

To make the interpretations universal between different DED setups, some generic terms like power density or corrected power density are used [46]. Using these terms will provide better insight into the process parameters of different DED setups that have different ranges for power, flow rate, and scan speed. Equation4.2 is used for the calculation of the power density. In this equation, laser power is divided by the scan speed and laser diameter. In order to include the flow rate inside the energy density term, energy density is divided by the flow rate forming equation 4.3 called corrected energy density. Figure 4.15 shows the correlation between dilution and corrected power density. Based on the figure, increasing the corrected power density value results in an increase in the dilution in the clads.

$$power\ density = \frac{laser\ power}{laser\ diameter \times scan\ speed} \tag{4.2}$$

$$corrected\ power\ density = \frac{laser\ power}{laser\ diameter \times scan\ speed \times flow\ rate} \tag{4.3}$$

4.5.4 Selection of the Parameters Based on Dilutions

The overall goal of obtaining the dilution values of the samples was to identify the process parameter window for the setup that would result in a clad with the desired specifications, including:

- good geometry
- minimum dilution with enough bonding to the substrate
- maximizing the size of the clad on top of the substrate's surface

As shown before, there is a local minimum in the dilution value at the power of 350 W that candidates it as proper laser power that provides enough bonding to the substrate while having a relatively good deposition rate. In the laser power of 350 W, flow rates of 0.5 and 1 g/min result in a relatively low deposition rate and dilution over 25%. The flow rate of 4 g/min, shown in figure 4.16b is not depositing good clad in terms of geometry and bonding compared to the flow rate of 3 g/min as presented in figure 4.16; the flow rate of 4 g/min at the laser power of 350 W is not letting the laser to pass the cloud of the metal powder and provide enough bonding to the substrate compared to the flow rate of 3 g/min. It is evident that the track at the flow rate of 4 g/min 4.16b is not having a uniform surface compared to the flow rate of 3 g/min as presented in figure 4.16a. This non-uniformity results in lower quality of the part when multiple layers are printed on top of each other. In summary, the flow rates of 2 and 3 g/min have accepted deposition rates while keeping good bonding to the substrate, with the dilution value of 21% and 5%, respectively. The dilution range of 5% to 25% is depositing clads that can satisfy the mentioned criteria and this

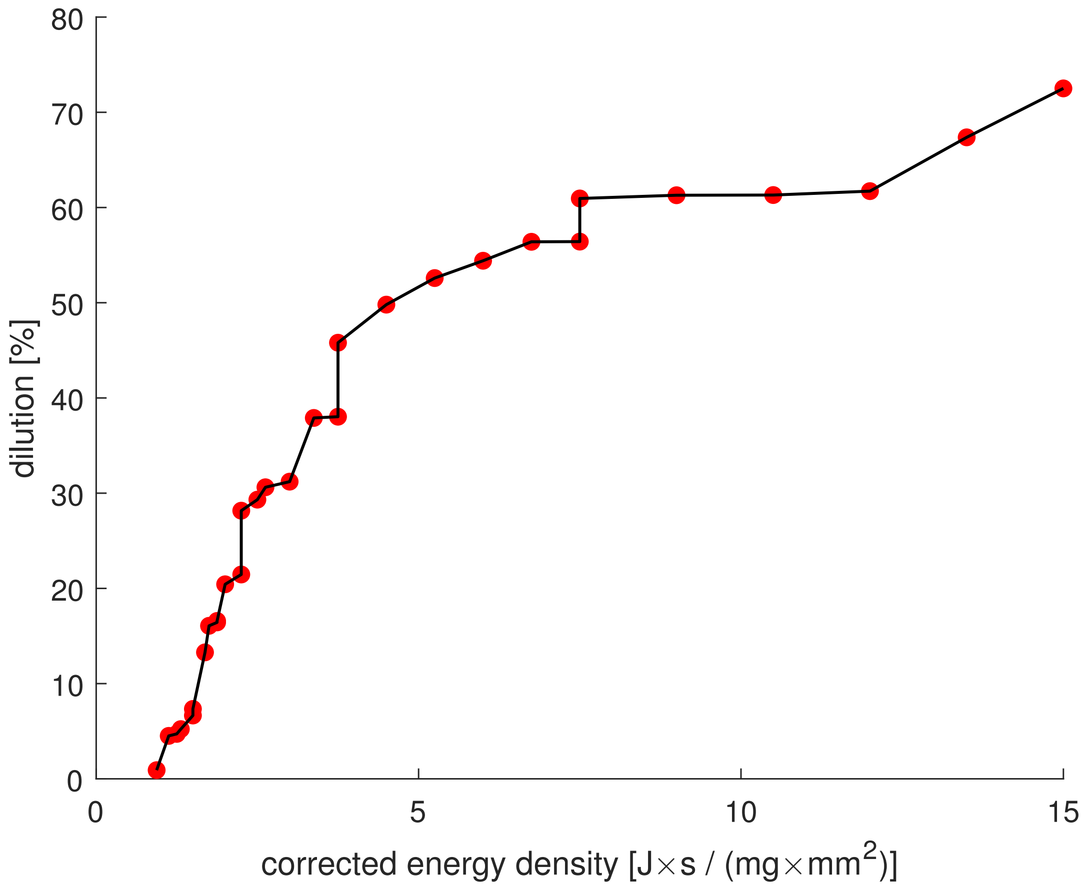

Figure 4.15: Variation of dilution at different corrected power densities.

range is chosen to be the proper dilution range of this setup. Therefore, the recommended process parameters can be used as the proper process parameters for the setup. Figure 4.17 shows the shape of the clads in all powers and flow rates.

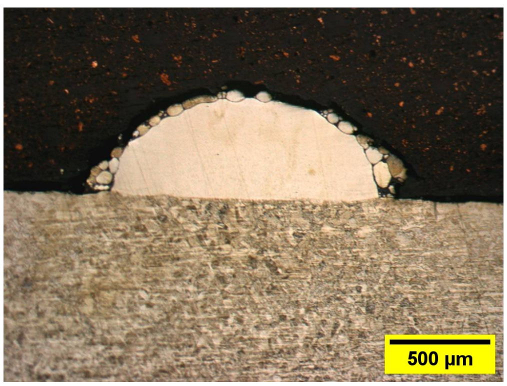

(a) Flow rate 3 g/min

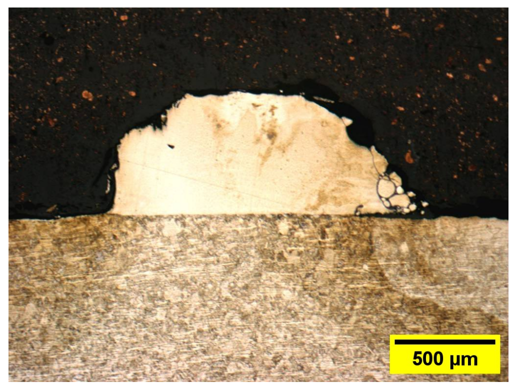

(b) Flow rate 4 g/min

Figure 4.16: Differene between the tracks deposited with flow rate of 3 g/min (a) and 4 g/min (b) in the laser power of 350 W.

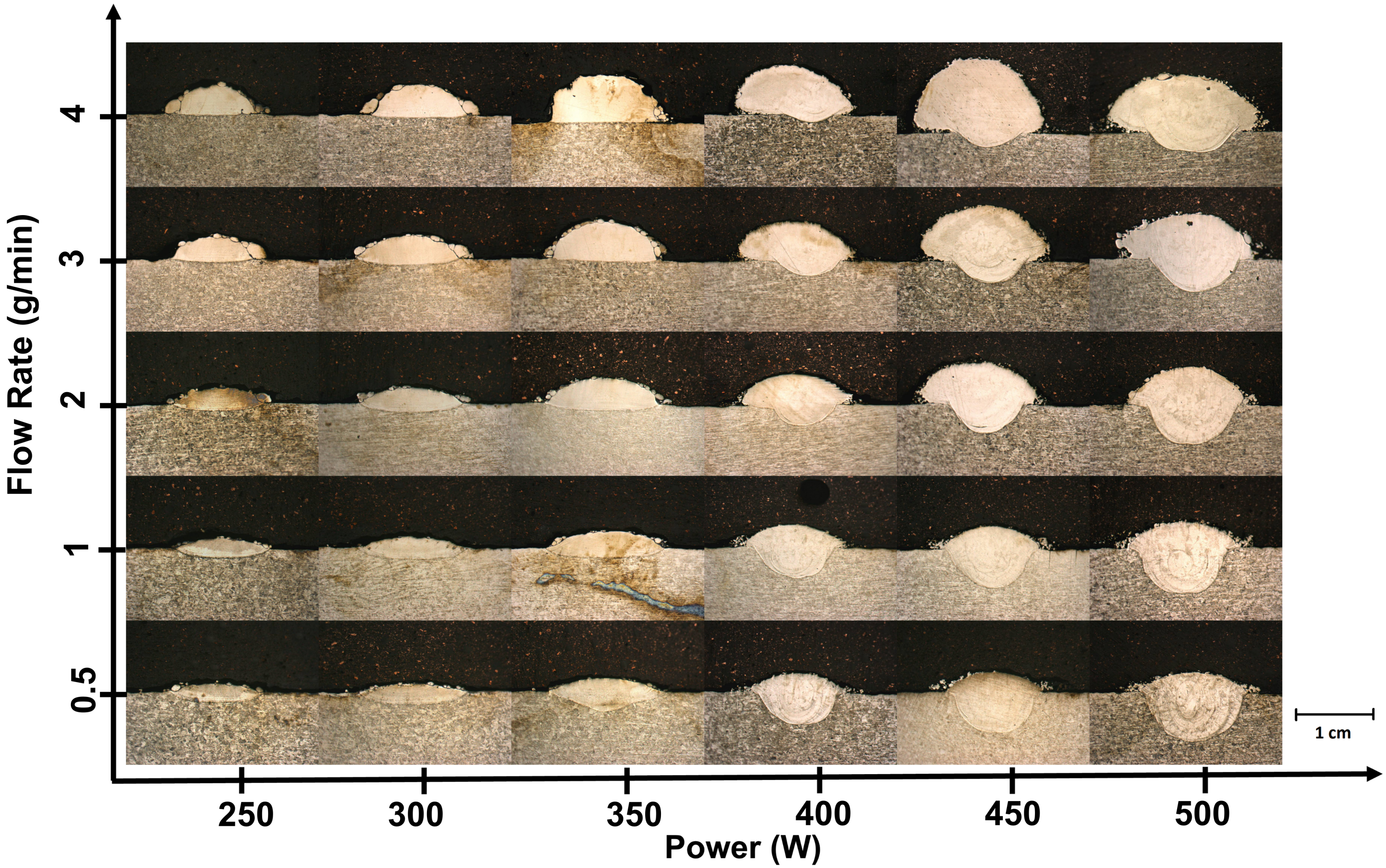

Figure 4.17: Variation of the dilution with respect to power for the flow rate of 2 g/min.

4.6 Conclusions

In summary, this chapter focuses on finding the proper process parameters for the experimental setup. The results of printing 150 tracks with different process parameters over the substrate were analyzed and among them, 30 tracks with more promising results were chosen. The cross-section of the selected tracks was ground, polished, and etched to visualize the melt pool and clad's height. A complete discussion over the variation of maximum heights of the clads, maximum depth of the melt pool, and dilution is done and based on them a proper dilution range (5% to 25%) and process window for the setup is determined. The process window recommends using the laser power of 350 W, the scan speed of 2 mm/s, and the flow rate of 2 or 3 g/min for this setup; these parameters deposit clads with a dilution ratio between 5 to 25%, which ensures good bonding while maximizing the deposition rate in the process.

Chapter 5

Predicting Melt Pool Temperature in DED Process Using Machine Learning

To predict the melt pool temperature in the laser-based DED process, physics-based models, including analytical and numerical methods, and data-driven models are developed. The determination of a closed-form analytical equation for the prediction of the melt pool temperature in the DED process is challenging. Analytical methods have been developed based on closed-form equations by solving welding boundary value problems to model temperature field in the DED process [30]. Because of the variations in the volume of the melt pool and mass of the metal powder during the process, as well as the uncertainties to the thermo-physical process, analytical models can't make reliable predictions and there will be discrepancies between analytical modeling and experiment [19, 43]. The other approach is using numerical models; these models are not accurate due to the lack of knowledge on the melt pool formation process, and simplifying assumptions established for the simulations [48]. Also, the accuracy of the model is highly dependent on the boundary conditions and meshing scheme [23]. Opposed to the analytical and numerical models, data-driven models can do the prediction based on experimental data with limited knowledge of the underlying physics. This chapter is focused on finding the best sequence models to be used in the ML pipeline for the prediction of the melt pool temperature in the DED process.

5.1 Temperature Data Acquisition, Processing, and Analysis

As mentioned in chapter 3, 2 sensors, including the IR camera and 2-wavelength pyrometer, were integrated into the DED setup. The IR camera captures the morphology of the melt pool and the 2-wavelength pyrometer read the top surface temperature of the melt pool. The focus of this thesis is on the prediction of the temperature of the melt pool and only the 2-wavelength pyrometer was used for data acquisition. The melt pool temperature was measured during the deposition process using the 2-wavelength pyrometer with a sampling rate of 0.01 seconds (100 Hz). At each sampling time, the pyrometer measures the maximum temperature over the surface of the melt pool. As a 2-wavelength pyrometer is used, the concern regarding the emissivity-based temperature reading will be resolved. The raw data of the melt pool temperature for the deposition of 6 layers of a thin wall is presented in Figure 5.1. The raw data contains high-frequency noise that is resulted from the data acquisition hardware in the pyrometer, blockage of the pyrometer's view by smoke and sparks coming out of the melt pool, etc. To remove the noise a moving average window with a length of 50 is applied to the data. Filtered data is shown in figure 5.2. There are some variations in the temperature of the melt pool that resulted from variations in the flow rate of the powder, variations in the delivered laser power to the melt pool, etc. Uni-directional printing pattern was used to print the thin wall; when the setup prints one layer, it stays for a bit longer (less than a second) at the end of the path until the laser turns off, resulting in accumulation of heat at that location and a spike in the melt pool temperature value at that position. In printing the first layer, the main heat transfer mode is conduction through the substrate that acts as the heat sink. But when the wall gets taller the conduction through the substrate will be less efficient because the melt pool is getting further from the substrate's surface, and heat transfer mode will shift toward convection over the surface of the thin wall, and radiation, that has lower efficiency compared to conduction from the substrate. Furthermore, as the idling time, which is the time between 2 consecutive layers to let the part cool down, is not enough to let the part get to the ambient temperature, when printing a thin wall, there will be a gradual increase in the temperature of the melt pool.

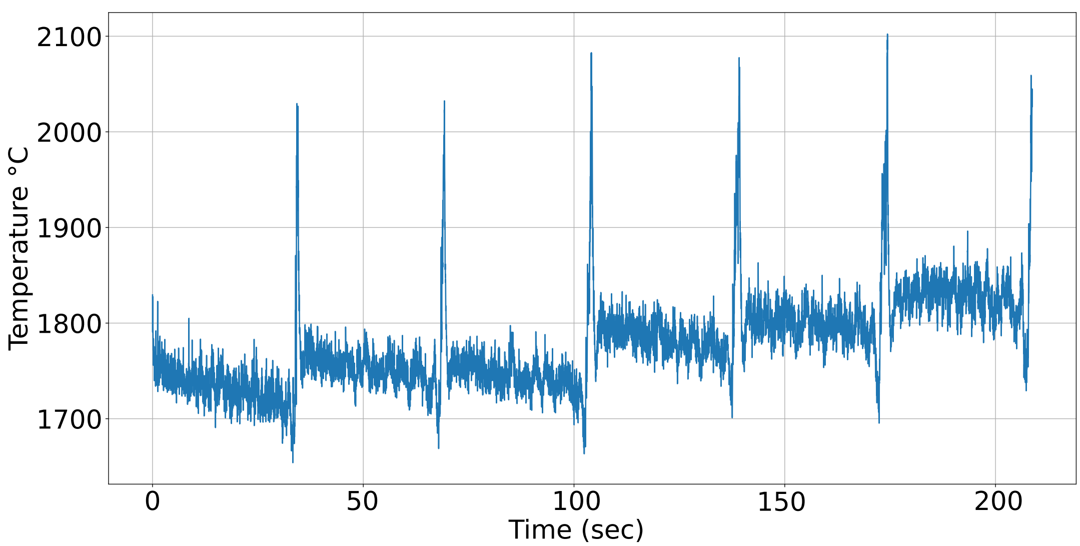

Figure 5.1: Raw temperature data for 6 layers.

5.2 Data Preparation

Using the raw data for training an ML model could decrease its performance, increase training time, and make the convergence unstable. Therefore, it is necessary to do data preparation before training, which involves normalizing the data, conversion to tensor data type, and windowing the

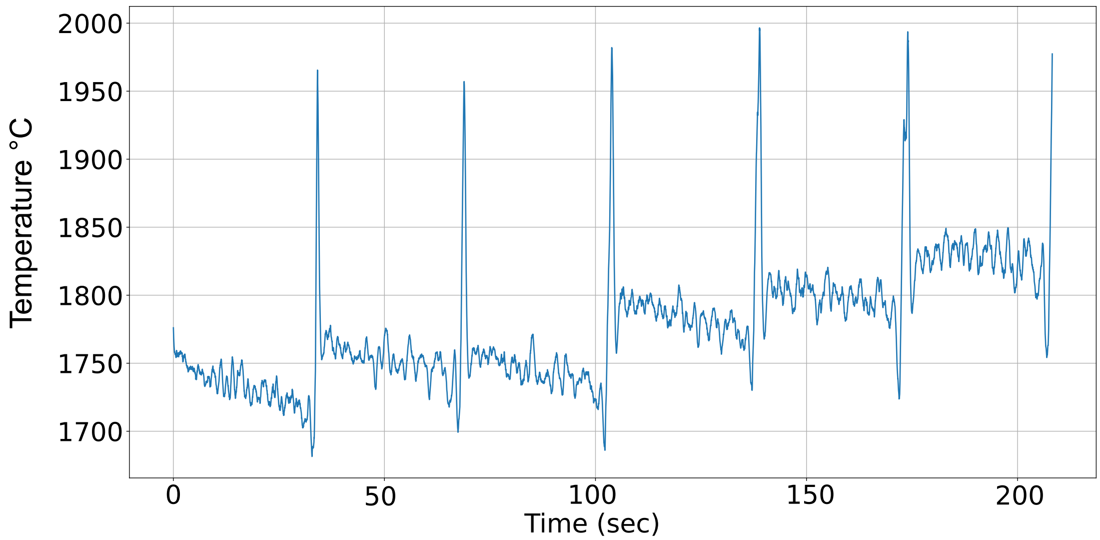

Figure 5.2: Temperature data after applying moving average filter.

data, with details explained in this section.

5.2.1 Normalizing the Data

It is important to normalize the melt pool temperature data before training an ML model as it helps the model to be more stable and converges sooner. Equation 5.1 shows the normalization formula, where μ is mean and σ is the standard deviation of the temperature. The mean value of the temperature data is 1777 °C, and the standard deviation is 47.6 °C.

$$normalized\,data = \frac{data - \mu}{\sigma} \tag{5.1}$$

5.2.2 Converting the Data to Tensor

The data is currently in the form of a Python array, but it needs to be converted into a tensor format to make the training faster. As GPUs have better performance in parallel computing compared to CPUs, converting the data to tensor and training over GPU will make the training of the ML model faster.

5.2.3 Splitting the Data

To assess the performance of the model, the data is split into 3 parts, including the training set, validation set, and the test set with the portion provided in table 5.1. The model is trained over the training data and evaluated at the end of each epoch on the validation data. Finally, after the training, the model is evaluated based on the test set. Figure 5.3 shows the ratios over the temperature data.

Table 5.1: Portions for the training, validation and test set.

Training set	70% of the temperature data
Validation set	20% of the temperature data
Test set	10% of the temperature data

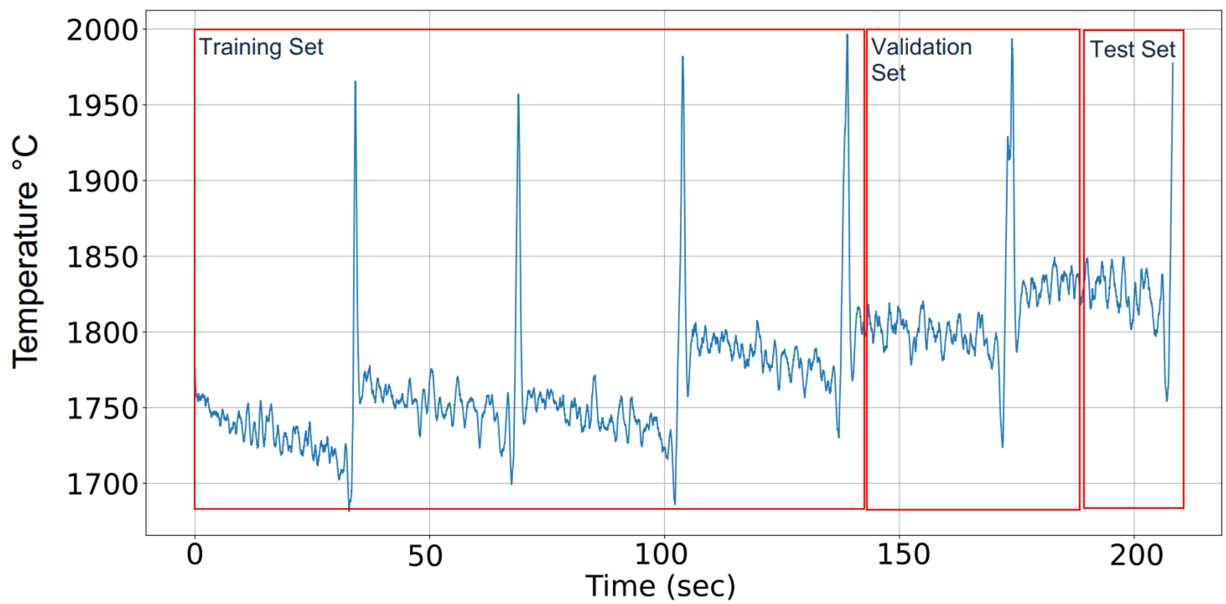

Figure 5.3: The training set, validation set, and test set of the temperature data used for training and testing the model.

5.2.4 Windowing the Data

In contrast to many ML applications where the model makes decisions solely based on the data at each time step, in sequence models, the ML model makes predictions based on the data that precedes the current time step. As a result, the data must be passed to the model in a window of data with a certain length at each time step.

The window size is one of the hyper-parameters in the training of a sequence model. It determines if the model is going to predict one step ahead, how many data points it needs from the previous time steps. Like all the hyper-parameters that are determined by trial and error for ML models, the size of the window is determined by trial and error. When the window size gets large, like 100 for this scenario, it will have a delay in predictions because it will have more focus on the long-term history, on the other hand, when it gets small, the model will do predictions similar to the baseline model as it can't consider the recent history in the input data. By doing iteration over the size of the window, the window size of 30 was selected. The first 29 data points are input data and the 30^{th} entry is the label data, that will be predicted. Figure 5.4 shows an example of creating windowed data. In this figure, the first 3 entries are chosen as input data and the 4^{th} entry is chosen as the label for them.

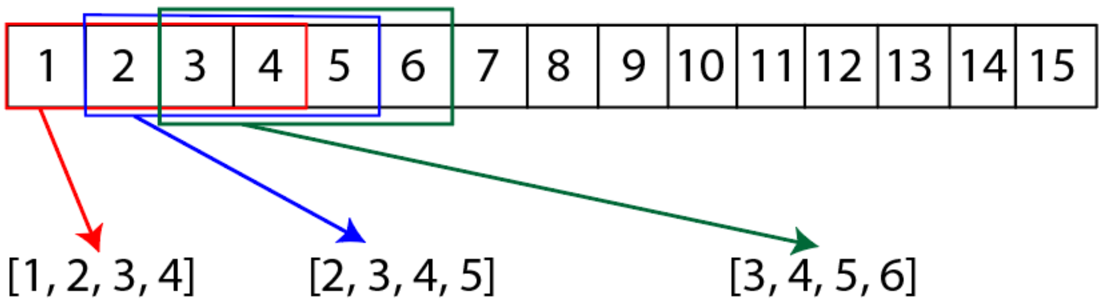

Figure 5.4: Sample of the windowed data with the window length of 4.

5.3 Machine Learning Models for Sequence Modeling

Many ML models are being used across various fields of research, including language modeling, object detection, image recognition, etc. All of these models are following the same approach for training; they are trained by feeding the input data into them, and they attempt to minimize the error by using cost functions and optimization methods such as stochastic gradient descent. These techniques allow the models to iteratively adjust their parameters to better fit the data, resulting in more accurate predictions.

In this thesis, the dataset consists of a sequence of melt pool temperature data that are correlated to each other. In other words, the value of the current data point is dependent on its history. This is the case in various examples such as the stock market and language models, where the data point at time t depends on the previous data points. Therefore, models with the ability to remember the history of the input data must be used. The list of models used for sequence modeling in the thesis is listed below.

- Baseline model
- Dense Neural Networks (DNN)

- 1D Convolutional Neural Networks (CNN)
- Recurrent Neural Networks (RNN)
- Gated Recurrent Unit (GRU)
- Long Short-Term Memory (LSTM)

There are many models available for each ML task and finding the best model is done through iteration. A baseline model is set and the performance of the rest of the models is compared to the baseline model. A detailed explanation of all the models used for iteration is provided in the rest of the section.

5.3.1 Baseline Model

The baseline model assumes that the melt pool temperature changes slowly and its variations are negligible. Thus, based on equation 5.2, the temperature prediction at time $t+1$, $\hat{y}(t+1)$, is considered equal to the true temperature value at time t, $y(t)$, which was measured by the 2-wavelength pyrometer at each time step. In other words, the measured temperature from the sensor is shifted one time step ahead to serve as the prediction of the temperature in the process. This baseline model will serve as a benchmark, against which the performance of other models will be compared.

$$\hat{y}(t+1) = y(t) \tag{5.2}$$

5.3.2 DNN Model

Dense models are one the most commonly used networks in different fields of ML like regression, image classification, pose estimation, object detection, etc. In these models sets of nodes, known as neurons, are stacked together and form a layer, all nodes of each layer are connected to all the nodes all the next layer, through parameters known as weights, to form dense neural networks. In the thesis, a dense model with 2 hidden layers, each containing 32 neurons, and an output layer with a single unit are used. The weights of the model are first randomly initialized and when the input model is fed, the model does the prediction and compares the result with the true value. Based on the difference between the prediction and the true value, the cost function, which is Mean Absolute Error (MAE) in this case, is calculated. Stochastic Gradient Descent (SGD) is used as the optimization approach to minimize the cost function and update the weights until the model converges to a desired performance. Figure 5.5 shows 3 different sections of the input temperature data at different time frames of the data. The model is using 29 data points to predict the label.

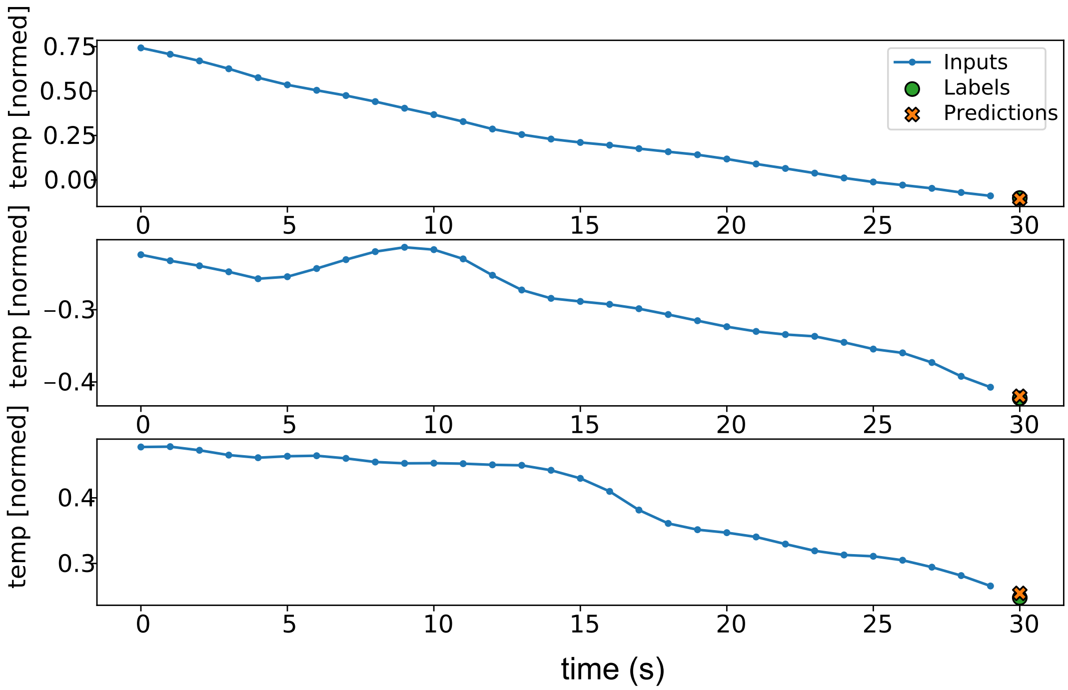

Figure 5.5: Prediction of the dense model at 3 different frames of the melt pool temperature data in the middle of layers.

5.3.3 CNN Model

CNN models are mainly used in ML applications related to computer vision. In CNN models, filters of a certain size are passed over the model to encode the data. Using the filters will decrease the size of the data and trainable parameters; also, they extract the features in the data which makes the training more efficient and faster. For the temperature data, the data is 1 dimensional; therefore, a 1-dimensional convolutional layer must be used. When a convolutional filter with the size of 29 passes over the data, it will encode all the 29 values into a single value and that single value is passed to a dense layer with 32 neurons and then a dense layer with a single neuron to do the prediction of the temperature. In training this model, the weights in the convolutional filters and the dense layers are initialized randomly. When the model is trained, the weights are updated until the model converges and predicts the results with the desired accuracy. The prediction results on the CNN model over 3 different time frames of the input data are shown in figure 5.6. As shown in the figure, the model is using the first 29 data to do the prediction for the 30th input. The convolutional filter takes one stride ahead in time does the prediction for the next time step, and so on.

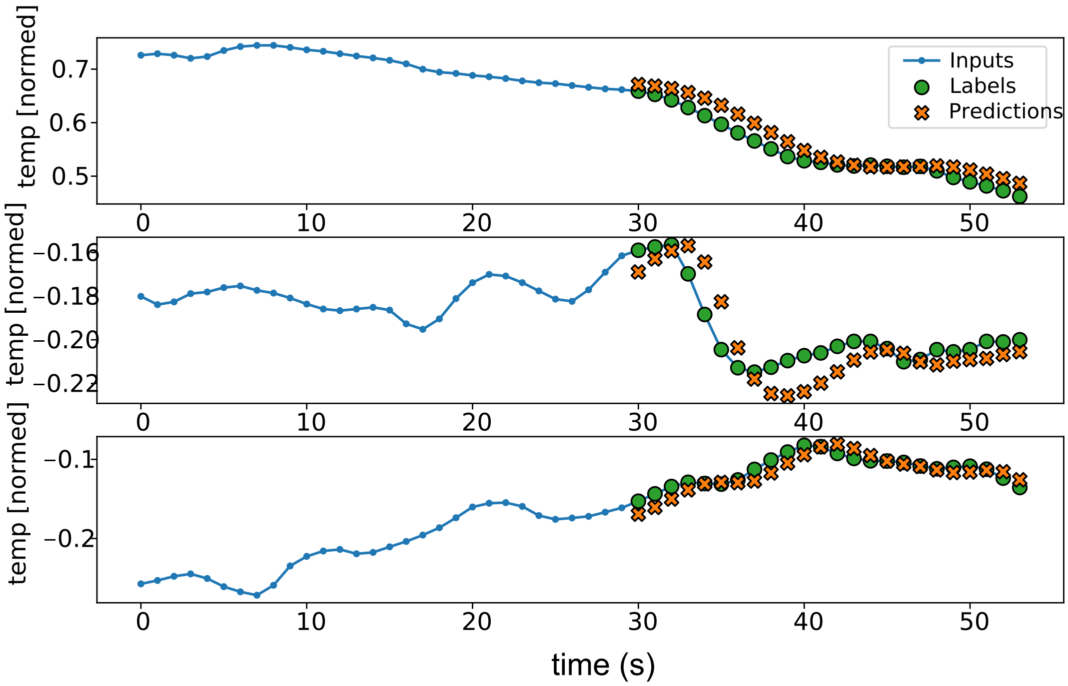

Figure 5.6: Prediction of the CNN model at 3 different frames of the melt pool temperature data in the middle of layers.

5.3.4 RNN Model

One of the weaknesses of using the dense and CNN models for the prediction of the sequential data is that they can't consider the history of the input data in their prediction and their prediction is only based on the fed data at each time step. To solve this weakness, models with additional parameters to remember the history of data are introduced to be used. One of the basic models used for the prediction of time series is RNN. The architecture of the model is shown in figure 5.7. The left side of the figure shows the compacted design of the model while the right-hand side shows its expansion over time. The window of the temperature data ($\mathrm{X}^{(<t>)}$) is fed to the model at each time step and the model is returning an output for each, which is the prediction of the next time step. This RNN model is called many-to-many, where the number of inputs is equal to the number of outputs. The parameters used in the RNN model are listed below [36]:

- $a^{<t>}$: This is the hidden state parameter. Contains information from the previous cell (history of temperature)
- $X^{<t>}$: This is the windowed temperature data fed into the model at each time step
- $\hat{y}^{<t>}$: This is the temperature prediction for the next time step

- b_a: The bias term for the hidden state
- b_y: The bias term for the output
- W_{ax}: The weight matrix for the inputs (shared across the sequence)
- W_{aa}: The weight matrix for the states (shared across the sequence)
- W_{ay}: The weight matrix for the output (shared across the sequence)

The governing equation in the RNN model is shown in equations 5.3 and 5.4. In equation 5.3, W_a is the combination of W_{aa} and W_{ax} which are stacked horizontally beside each other. The activation function, g, is tanh. At each step of the iteration, $a^{<t>}$ and $y^{<t>}$ are computed in the forward direction to make a prediction and then the prediction is compared to the actual value to evaluate the cost function for each output based on equation 5.5. Based on the sum of the cost function in equation 5.6, the backpropagation is done over the model to minimize the cost function by the SGD optimization technique. After each backpropagation, the weights, that were initialized randomly in the beginning, are updated. This process takes place over and over until an acceptable value for accuracy is obtained and the cost function is minimized.

$$a^t = g(W_a[a^{t-1}, X^t] + b_a) \tag{5.3}$$

$$\hat{y}^{<t>} = g(W_{ya}a^t + b_y) \tag{5.4}$$

$$\mathcal{L}^{<t>}(\hat{y}^{<t>}, y^{<t>}) = -y^{<t>}\log(\hat{y}^{<t>}) - (1 - y^{<t>})\log(1 - (\hat{y}^{<t>}) \tag{5.5}$$

$$\mathcal{L} = \sum_{t=1}^{T_y} \mathcal{L}^{<t>}(\hat{y}^{<t>}, y^{<t>}) \tag{5.6}$$

The advantage of using RNN is its simplicity which results in lower computation cost compared to the more complex sequence models, like GRU and LSTM, but its disadvantage is that it can only consider the state from the previous cell and has a short-term memory; thus, it is not expected from RNN to remember events from a long time ago. The prediction results of a model with 2 hidden layers, each with 32 RNN units, followed by a dense layer with a single neuron over 3 different frames of the temperature data is shown in figure 5.8. Based on the figure, it is evident that the model is able to estimate the temperature at each time step that is close to the true value.

5.3.5 GRU Model

One of the weaknesses of RNN models is their short-term memory that results in vanishing gradient because of their simple structure compared to GRU and LSTM that is not able to remember the

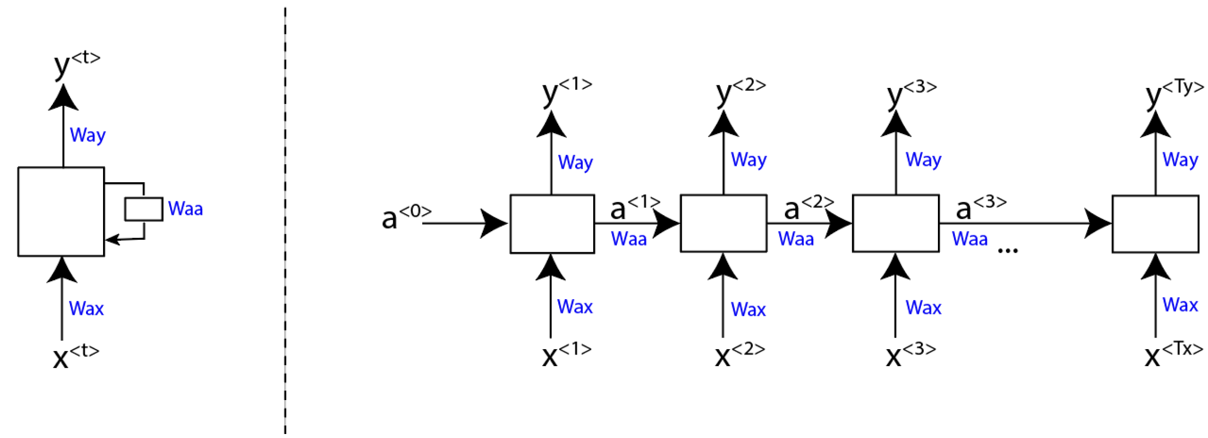

Figure 5.7: RNN architecture.

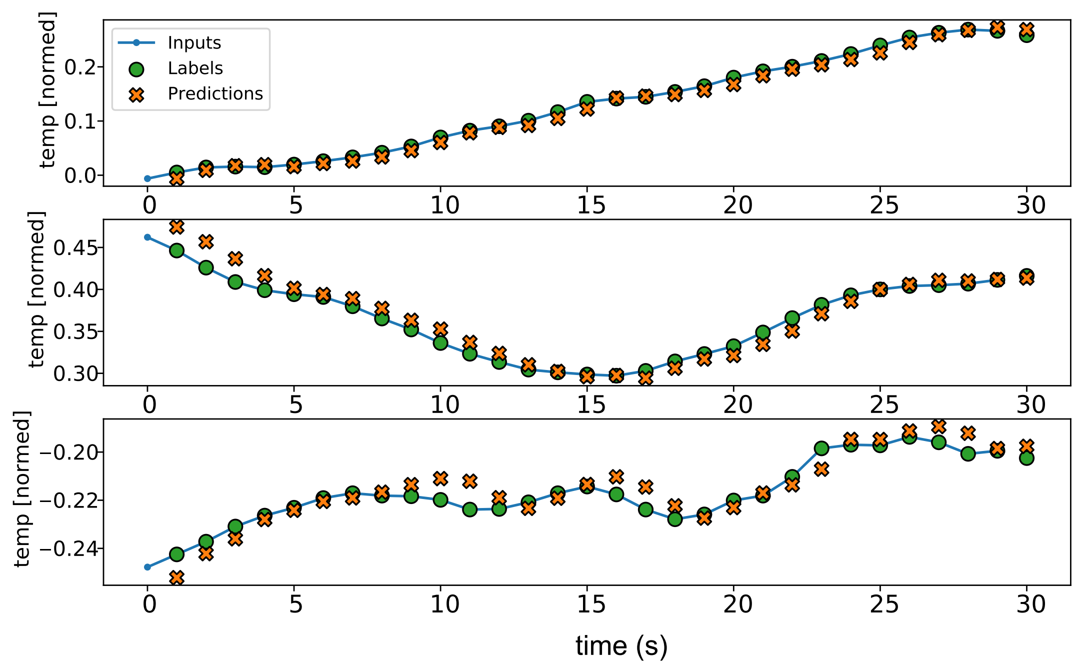

Figure 5.8: Prediction results of RNN model at 3 different frames of the melt pool temperature data in the middle of layers.

data from a long time ago. In the vanishing gradient, the gradient of the weights gets smaller and close to zero; consequently, it will not be able to update the weights of the model and improve the prediction accuracy. To overcome this weakness, more complex models like GRU and LSTM are developed. Both the GRU and LSTM models have some additional gates to remember the data for a longer time. The gates in the GRU model are [7]:

- Relevance Gate (Γ_r)
- Update Gate (Γ_u)

The other parameters used in the GRU model are

- $C^{<t>}$: The cell state at each time step
- $\tilde{C}^{<t>}$: The possible candidate for $C^{<t>}$
- b_c: The bias term for the cell state
- b_r: The bias term for the relelance gate
- b_u: The bias term for the update gate
- W_c: The weight matrix for cell state
- W_r: The weight matrix for relevance gate
- W_u: The weight matrix for update gate
- $\hat{y}^{<t>}$: The prediction of the cell

In the RNN architecture shown in figure 5.7, each RNN gets the state variable from the previous cell and therefore, in long sequences, it will not remember the information from the beginning of the sequence. Unlike the RNN model, in GRU architecture shown in figure 5.9, there is some additional gate that controls the flow of the information from the previous cells; these gates help to remember the information from the beginning of the sequence for future predictions. At each time step in the GRU model, a possible candidate for the cell state $\tilde{C}^{<t>}$ is computed that contains the most recent information about the sequence by equation 5.7 containing the value of the relevance gate, previous step cell's memory content $C^{<t-1>}$, current input, and the bias term. The gates in the GRU model decide whether to keep the previous cell memory or update the cell memory to the candidate cell memory. These gates and their functionality are explained in the following.

$$\tilde{C}^{<t>} = \tanh(W_c[\Gamma_r * C^{<t-1>}, X^{<t>}] + b_c) \tag{5.7}$$

Update Gate

In the GRU model, the information from the previous cells is stored in cell memory $C^{<t>}$. At each time step, the update gate decides whether to update the cell memory to the possible candidate cell memory ($\tilde{C}^{<t>}$). The decision for the update gate is done by equation 5.8 that is computed based on the previous cell memory, the current input, and the bias term inside the sigmoid function shown in equation 5.9. The value of the sigmoid function is close to 0 or 1.

$$\Gamma_u = \sigma(W_u[C^{<t-1>}, X^{<t>}] + b_u) \tag{5.8}$$

$$sigmoid\, function = \frac{1}{1 + \exp(-x)} \tag{5.9}$$

Relevance Gate

This gate is used to consider the relevance between the previous cell memory $C^{<t-1>}$ and the possible candidate cell memory ($\tilde{C}^{<t>}$). The relevance gate Γ_r is computed by equation 5.10 based on the previous cell memory, the current input, and the bias term.

$$\Gamma_r = \sigma(W_r[C^{<t-1>}, X^{<t>}] + b_r) \tag{5.10}$$

Finally, after calculation of the update gate, relevance gate, and the candidate cell memory, the cell's memory content is updated based on equation 5.11, which is equal to the prediction. Next, like the RNN model, the loss function is calculated and minimized through optimization to update the weight of the model.

$$C^{<t>} = \Gamma_u \times \tilde{C}^{<t>} + (1 - \Gamma_u) \times C^{<t>} \tag{5.11}$$

The prediction results of a model with 2 hidden layers, each with 32 GRU units, followed by a dense layer with a single neuron over 3 different frames of the temperature data is shown in figure 5.10. The prediction results closely follow the true values that make this model a good candidate for data-driven modeling.

5.3.6 LSTM Model

One of the other sequence models with the ability to remember the history of the data when doing the prediction is the LSTM model. LSTM models are frequently used in natural language processing that any sentence can be given to the model, and the model understands and return a response to it like ChatGPT. The LSTM model is similar to the GRU model with more gates and added computational complexity. Figure 5.11 shows the architecture and flow of the data in the LSTM model. The parameters used in the LSTM model are listed below [36]:

- $C^{<t>}$: the cell state at each time step
- $a^{<t>}$: hidden state vector known as the output vector of the LSTM unit, computed by equation 5.17
- $C^{\tilde{<t>}}$: the possible candidate for $C^{<t>}$

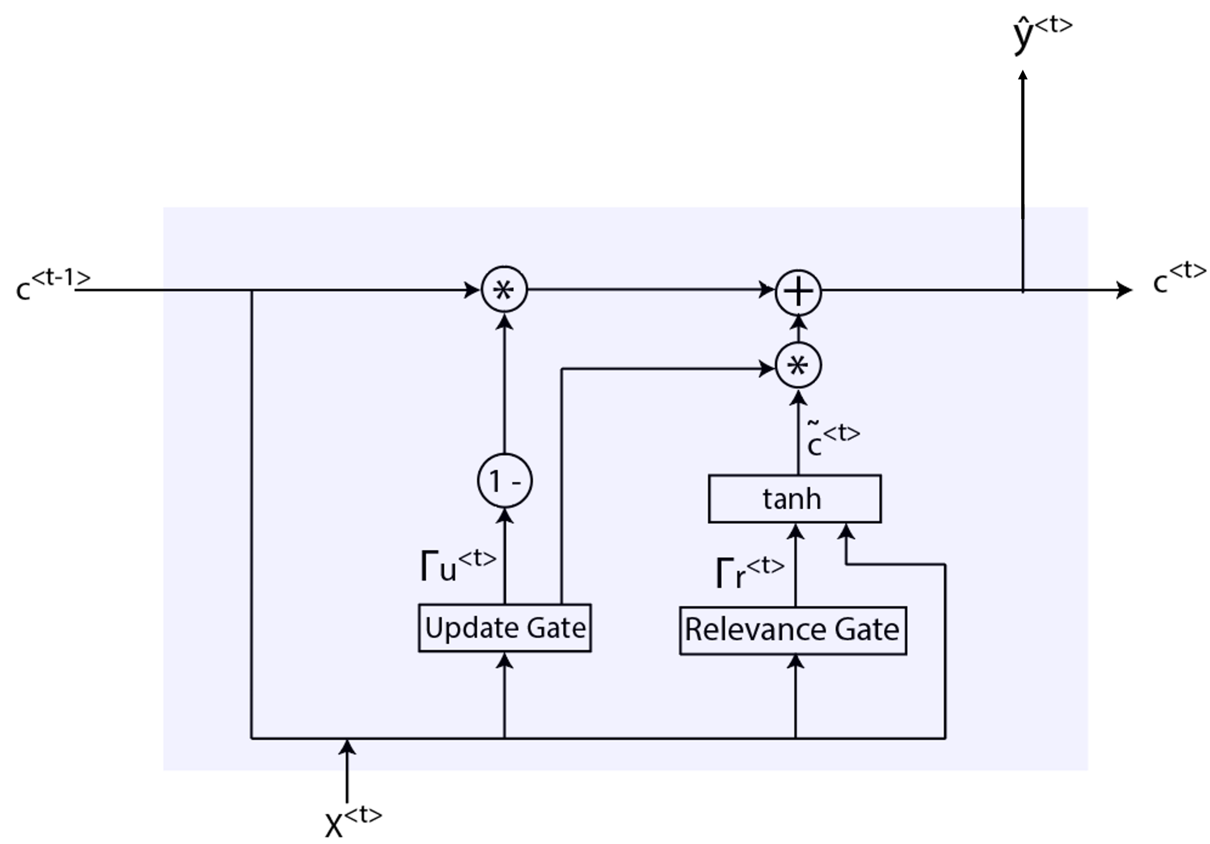

Figure 5.9: GRU architecture.

- W_c: the weight matrix for the cell state
- W_f: the weight matrix for forget gate
- W_u: the weight matrix for the update gate
- W_o: the weight matrix for the output gate
- $\hat{y}^{<t>}$: the prediction of the cell

In the LSTM model, the possible candidate for the cell state is computed at each time step by equation 5.12 by the hidden state vector and the current input. Unlike the GRU model, the LSTM model has an additional gate called forget gate (Γ_f) computed by equation 5.14. The forget gate and the update gate decide on updating the cell state based on the candidate cell state by equation 5.16. The LSTM unit outputs the prediction which is equal to the computed cell state.

$$\tilde{C}^{<t>} = \tanh(W_c[a^{<t-1>}, X^{<t>}] + b_c) \tag{5.12}$$

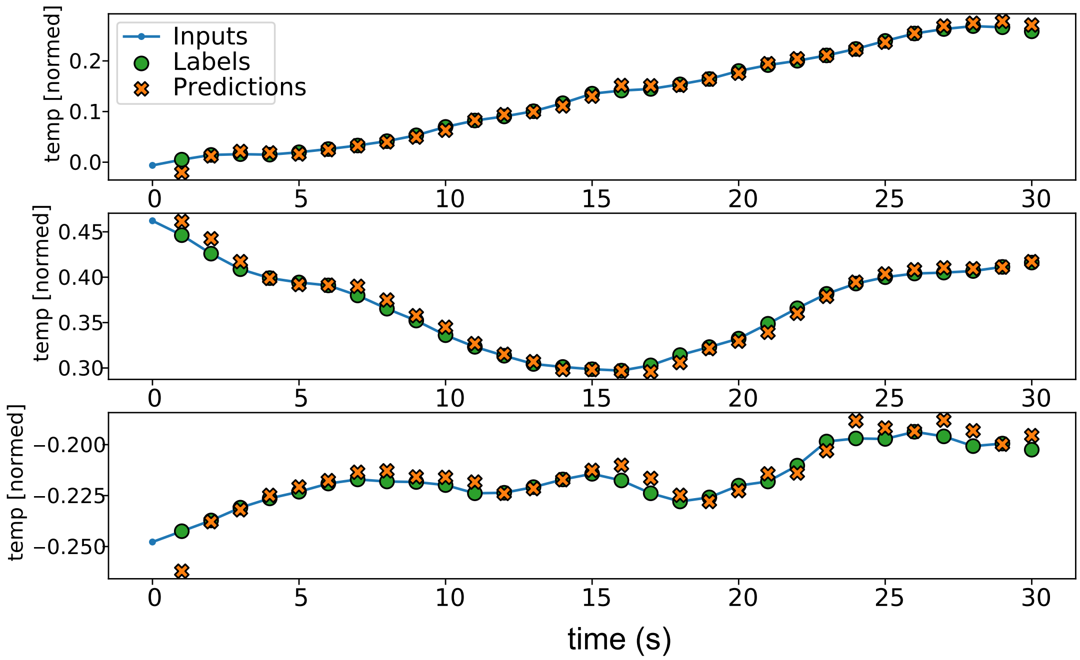

Figure 5.10: Prediction results of GRU model at 3 different frames of the melt pool temperature data in the middle of layers.

$$\Gamma_u = \sigma(W_u[a^{<t-1>}, X^{<t>}] + b_u) \tag{5.13}$$

$$\Gamma_f = \sigma(W_f[C^{<t-1>}, X^{<t>}] + b_f) \tag{5.14}$$

$$\Gamma_o = \sigma(W_o[C^{<t-1>}, X^{<t>}] + b_o) \tag{5.15}$$

$$C^{<t>} = \Gamma_u * \tilde{C}^{<t>} + \Gamma_f * C^{<t-1>} \tag{5.16}$$

$$a^{<t>} = \Gamma_o * \tanh(C^{<t>}) \tag{5.17}$$

The prediction results of a model with 2 hidden layers, each with 32 LSTM units, followed by a dense layer with a single neuron over 3 different frames of the temperature data is shown in figure 5.12. Based on the figure, the predicted values can closely follow the variations in the temperature that make this model a proper candidate for data-driven modeling of the temperature.

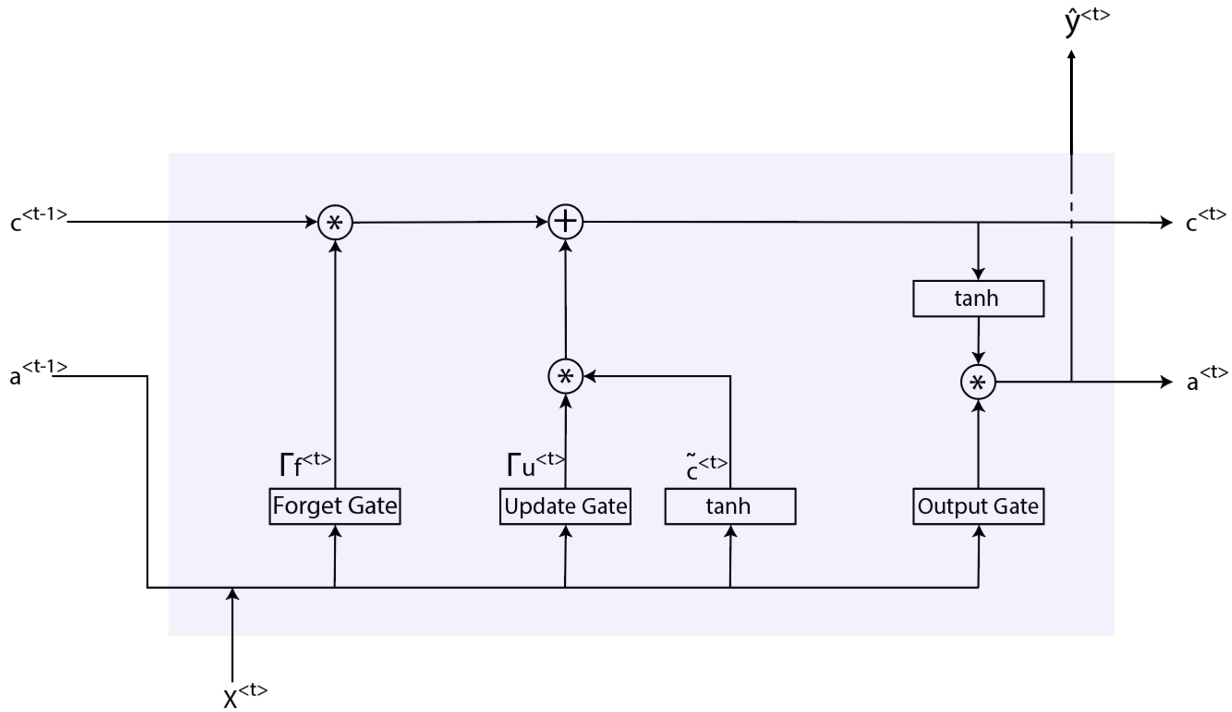

Figure 5.11: LSTM architecture.

5.3.7 Comparison on the Prediction among Different Models

To check the performance of models, the Mean Absolute Error (MAE) between the predicted and the true value of the temperature was calculated based on equation 5.18 on the test set and the validation set, together around 6000 data points and results are shown in figure 5.13. Based on the figure, all of the ML methods are performing better than the baseline model, that makes ML approaches a good candidate for temperature prediction and data-driven modeling in the DED process. By comparing the MAE of the baseline model and the sequence models with better memory, like LSTM and GRU, it is evident that these sequence models are having about 20 times better performance based on the MAE values on the validation and test set. This better performance makes them good candidates to be used inside the ML pipeline for prediction of the melt pool temperature.

$$MAE = \frac{\sum_{i=1}^{n} |\hat{y}^{<t>} - y^{<t>}|}{n} \tag{5.18}$$

5.4 Prediction Results

Up to this point, the working principle of different ML models that are commonly being used for sequential model predictions was discussed and various ML models, like the dense model, 1D CNN,

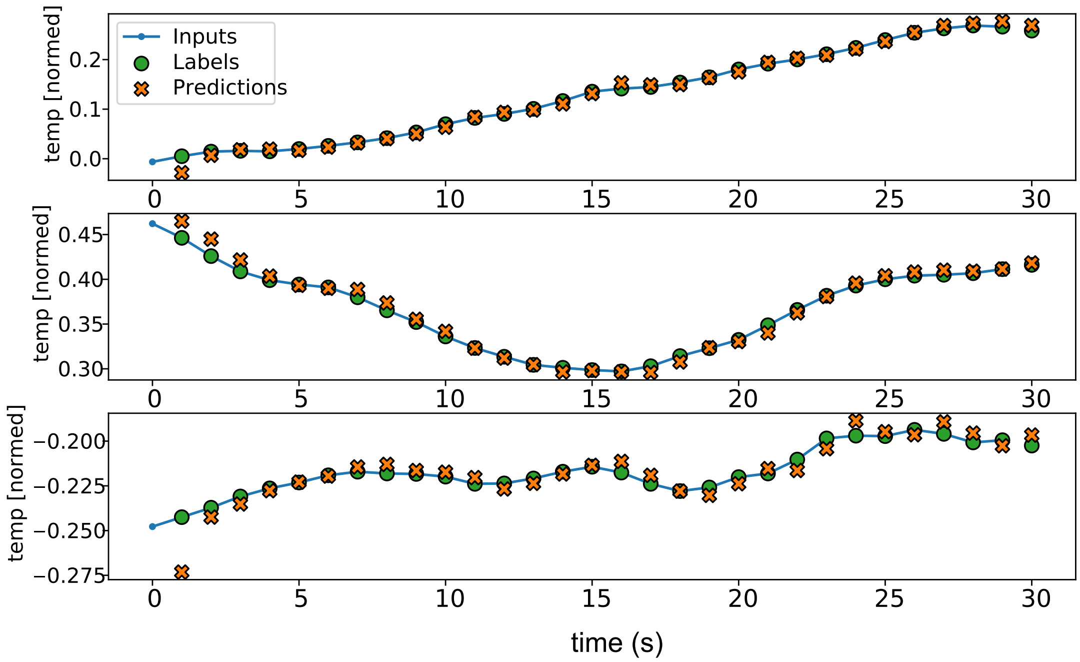

Figure 5.12: Prediction results of LSTM model at 3 different frames of the melt pool temperature data in the middle of layers.

RNN, GRU, and LSTM were trained over the model to check their performance. Among them, GRU and LSTM models were shown that are working better over the temperature data compared to the rest of the models. Between these 2 models, the LSTM model that has more gates for remembering the history of the data is chosen to be implemented into the ML pipeline for prediction of the temperature.

The ML pipeline uses the LSTM model tested in section 5.3.6. This model is trained over the data for 50 epochs and the prediction results of the model over the validation and test set, which was not seen by the model during the training, are shown in figure 5.14. Figure 5.15 shows the prediction results from Zhang et al. [53]. They did the implementation of XGBoost and LSTM models for the prediction of the temperature in the DED process and concluded that the LSTM model is having better performance compared to the XGBoost model. In their model, as they are only using one unit of LSTM and not choosing the proper hyper-parameters for the model, their prediction results are not as accurate as the model developed in this thesis. The implemented model in this thesis not only is able to predict the melt pool temperature trend, but also can estimate the fluctuation in the temperature that is resulted due to the variation of the delivered laser power and the flow rate to the melt pool. Comparison between figure 5.14 and figure 5.15 is shown the

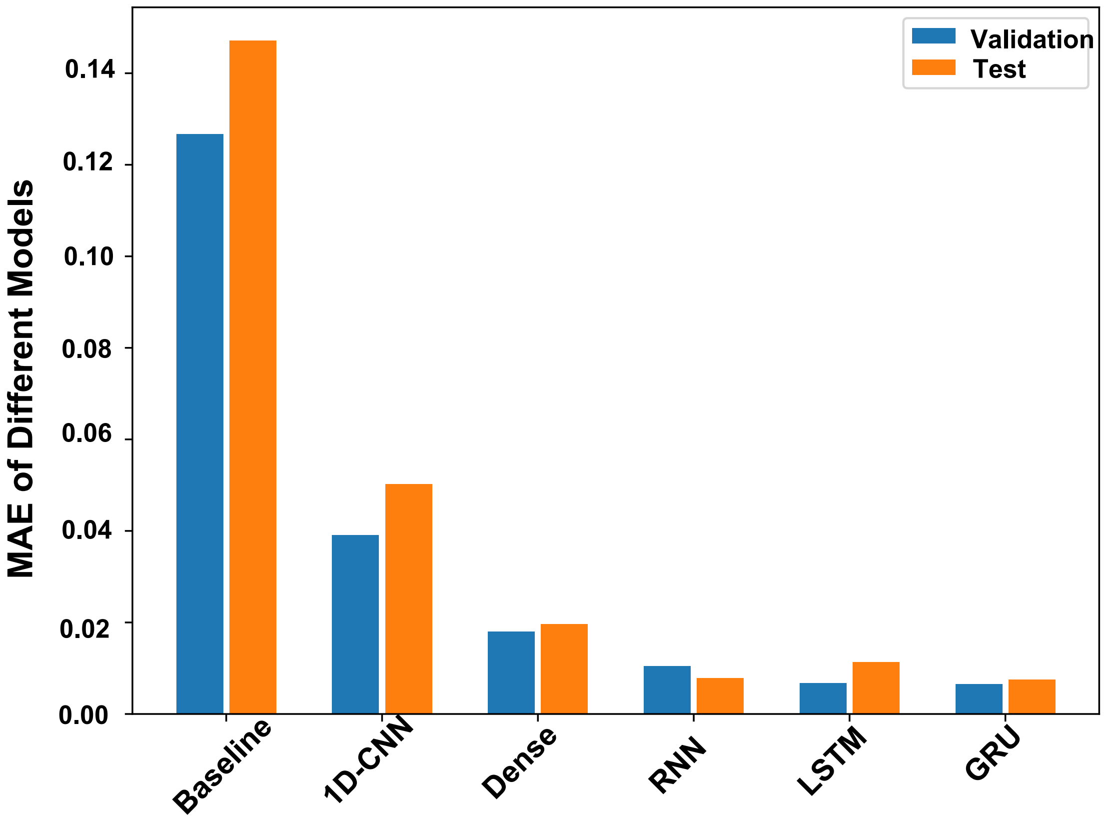

Figure 5.13: Comparison in performance of different models.

superiority of the model developed in this thesis.

5.5 Conclusions

Due to the challenges and discrepancies in the prediction of the melt pool temperature between the physics-based models, i.e., analytical and numerical models, and the experiments in the DED process, an ML-based approach was chosen for the prediction of temperature in the DED process. As the current temperature of the melt pool is dependent on its history, ML models with the ability to consider the history of the data were chosen to do trials and determine the best model with proper hyper-parameters among them. Several models, including the dense model, 1D-CNN, RNN, GRU, and LSTM were trained over the melt pool temperature data and their performance on the validation set and the test set were analyzed. Among these models, GRU and LSTM did better performance in the prediction of temperature compared to the others because of the additional gates

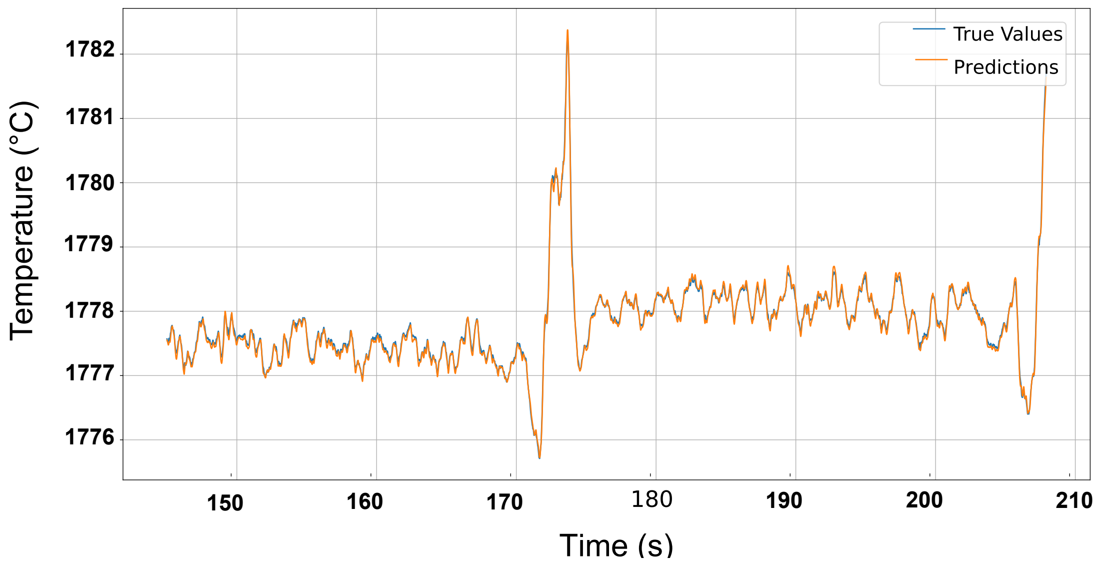

Figure 5.14: Prediction of the developed model over the validation and test set.

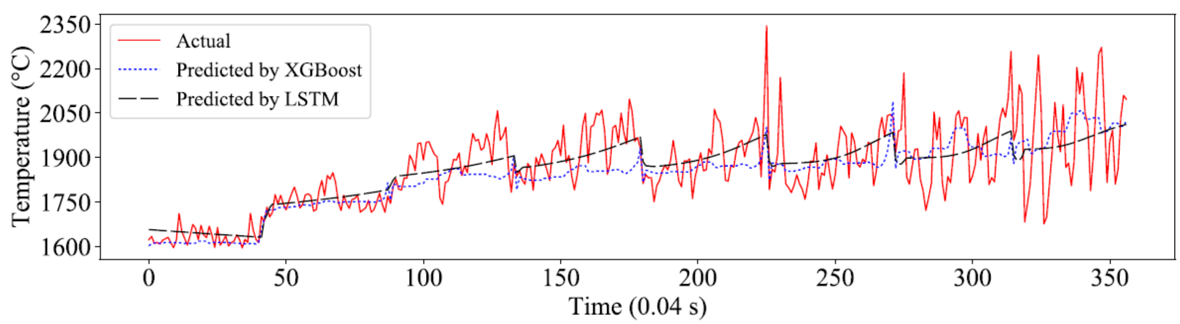

Figure 5.15: Performance of the model proposed by Zhang et al. [53] to predict the melt pool temperature in DED process.

used inside these models for remembering the sequence of the data. Between LSTM and GRU, LSTM has more gates for remembering the sequence in data and is widely used for different ML applications related to sequences; therefore, the LSTM model was chosen to be implemented into the ML pipeline for the prediction of the temperature. After training the model, it was evaluated over the test set and results were compared to the existing studies in the data-driven prediction of the melt pool. The trained model shows better performance in the prediction of the temperature and can predict the trend and fluctuations in the melt pool temperature data during the printing of a 6-layer thin wall.

Chapter 6

Conclusions and Future Works

AM is opening new opportunities in the manufacturing industry due to its unique capabilities in manufacturing complex parts, building parts with unique material properties, repairing existing parts, etc. Despite all the advantages, this process is suffering from a lack of repeatability and defects that hinders it from entering critical industries such as aerospace.

In this thesis, a laser generator, deposition head, and powder feeder were integrated into an existing 3-axis motion stage to make an in-house laser-based DED setup. Proper sensors, including an IR camera and a 2-wavelength pyrometer, were purchased and integrated into the setup to monitor the morphology and temperature of the melt pool during the DED process. Next, open-source software was developed with the ability to control the laser generator and sensors to facilitate controlling the process by the feedback received from the sensors for future studies. Moreover, as temperature measurement with the IR camera is highly dependent on the emissivity of the material, the software uses the temperature reading from the 2-wavelength pyrometer to calibrate the IR camera's temperature. Finally, to test the setup, a thin wall with multiple layers was printed and possible reasons for the geometrical defects in the thin wall were discussed.

After integrating the setup and making it ready to use, a set of experiments was designed to determine the proper process window for the machine that results in clads with good bonding to the substrate and proper geometry. In the experiment, 150 single-layer clads were printed over the substrate and after polishing and etching the cross-section of the selected ones, they were analyzed under an optical microscope. The purpose of this study was to find the correlation between the main process parameters, like laser power, scan speed, and flow rate, with the clad's geometrical properties including height, depth, and dilution. Next, based on the assessments on the clads, the laser power of 350 W, the scan speed of 2 mm/s, and flow rates of 2 and 3 g/min were chosen as the process window of the DED setup that results in the deposition of clads with good bonding, geometry, and dilution ratios between of 5% to 25%, which is determined as the proper range for this setup and used materials.

The DED process has a hard-to-model nature because of the multi-physics phenomena, like melting and solidification, happening during the process. Analytical and numerical models have low accuracy in estimating the melt pool temperature during the DED process because of the simplifying assumptions established for their development which results in discrepancies between the model and experiment; therefore, an ML-based data-driven model for the prediction of temperature in the DED process is developed to do the prediction based on the experimental temperature data. The temperature data in printing a 6-layer thin wall was captured from a 2-wavelength pyrometer and after preprocessing over the data it was fed as the input to various ML models, including dense neural networks, 1D-CNN model, RNN, GRU, and LSTM. Among these models, LSTM and GRU show superior performance compared to the rest of the models in remembering the history of the data and doing predictions. As the LSTM model can more effectively store and access the long-term dependencies using a special type of memory cell and gates compared to the GRU model, the LSTM model was selected for the development of the ML pipeline in the prediction of the melt pool temperature. The developed model shows better performance compared to the existing data-driven models for the prediction of melt pool temperature.

This work set the basis for future studies and experiments conducted in our lab. The following topics can be explored further as the continuation of this thesis:

- In data-driven approaches having more data always leads to creating more complex models with more capabilities. By having more data, instead of predicting one time step ahead in the future, more time steps ahead, like 5 or 10, can be predicted, and later this model can be integrated into the software for controlling the temperature. As the ML model can predict the temperature sooner in the future, it will be an aid for the inherent latency in the DED process and the laser power can be set accordingly to keep the melt pool temperature in a certain range
- The microstructure of the clads can be investigated to find the correlation of the process parameters with the microstructure of the printed clads
- The IR camera can capture the morphology and temperature distribution of the melt pool; based on the IR images, a data-driven model can be developed to monitor the temperature distribution and melt pool shape in the process and do defect detection based on the melt pool morphology and temperature distribution

Bibliography

[1] TE Abioye, J Folkes, and AT Clare. A parametric study of inconel 625 wire laser deposition. *Journal of Materials Processing Technology*, 213(12):2145–2151, 2013.

[2] LA Andreevskikh, AA Drozdov, AL Mikhailov, Yu M Samarokov, OA Skachkov, and AA Deribas. Producing bimetallic steel-copper composites by explosive welding. *Steel in Translation*, 45:84–87, 2015.

[3] Clint Atwood, Michelle Griffith, Lane Harwell, Eric Schlienger, Mark Ensz, John Smugeresky, Tony Romero, Don Greene, and Daryl Reckaway. Laser engineered net shaping (lens™): A tool for direct fabrication of metal parts. In *International congress on applications of lasers & electro-optics*, volume 1998, pages E1–E7. Laser Institute of America, 1998.

[4] Shyam Barua, Frank Liou, Joseph Newkirk, and Todd Sparks. Vision-based defect detection in laser metal deposition process. *Rapid Prototyping Journal*, 20(1):77–85, 2014.

[5] Benjamin Bax, Rohan Rajput, Richard Kellet, and Martin Reisacher. Systematic evaluation of process parameter maps for laser cladding and directed energy deposition. *Additive Manufacturing*, 21:487–494, 2018.

[6] Prveen Bidare, Aldi Mehmeti, Amaia Jiménez, Sheng Li, Chris Garman, Stefan Dimov, and Khamis Essa. High-density direct laser deposition (dld) of cm247lc alloy: microstructure, porosity and cracks. *The International Journal of Advanced Manufacturing Technology*, 120(11-12):8063–8074, 2022.

[7] Junyoung Chung, Caglar Gulcehre, KyungHyun Cho, and Yoshua Bengio. Empirical evaluation of gated recurrent neural networks on sequence modeling. *arXiv preprint arXiv:1412.3555*, 2014.

[8] GP Dinda, AK Dasgupta, and J Mazumder. Evolution of microstructure in laser deposited al–11.28% si alloy. *Surface and Coatings Technology*, 206(8-9):2152–2160, 2012.

[9] Charalabos Doumanidis and Yong-Min Kwak. Geometry modeling and control by infrared and laser sensing in thermal manufacturing with material deposition. *J. Manuf. Sci. Eng.*, 123(1):45–52, 2001.

[10] M Froend, S Riekehr, N Kashaev, B Klusemann, and J Enz. Process development for wire-based laser metal deposition of 5087 aluminium alloy by using fibre laser. *Journal of Manufacturing Processes*, 34:721–732, 2018.

[11] Myriam Gharbi, Patrice Peyre, Cyril Gorny, Muriel Carin, Simon Morville, Philippe Le Masson, Denis Carron, and Rémy Fabbro. Influence of various process conditions on surface finishes induced by the direct metal deposition laser technique on a ti–6al–4v alloy. *Journal of materials processing technology*, 213(5):791–800, 2013.

[12] Brian T Gibson, Yashwanth Kumar Bandari, Bradley S Richardson, William C Henry, Emma J Vetland, Tayler W Sundermann, and Lonnie J Love. Melt pool size control through multiple closed-loop modalities in laser-wire directed energy deposition of ti-6al-4v. *Additive Manufacturing*, 32:100993, 2020.

[13] Qian Guo, Suiyuan Chen, Mingwei Wei, Jing Liang, Changsheng Liu, and Mei Wang. Formation and elimination mechanism of lack of fusion and cracks in direct laser deposition 24crnimoy alloy steel. *Journal of Materials Engineering and Performance*, 29:6439–6454, 2020.

[14] Lijun Han, Frank W Liou, and Srinivas Musti. Thermal behavior and geometry model of melt pool in laser material process. 2005.

[15] Francisco P Jeantette, David M Keicher, Joseph A Romero, and Lee P Schanwald. Method and system for producing complex-shape objects, April 4 2000. US Patent 6,046,426.

[16] Suyog Jhavar, Neelesh K Jain, and CP Paul. Development of micro-plasma transferred arc (μ-pta) wire deposition process for additive layer manufacturing applications. *Journal of Materials Processing Technology*, 214(5):1102–1110, 2014.

[17] SM Kelly and SL Kampe. Microstructural evolution in laser-deposited multilayer ti-6al-4v builds: Part i. microstructural characterization. *Metallurgical and Materials Transactions A*, 35:1861–1867, 2004.

[18] Mojtaba Khanzadeh, Sudipta Chowdhury, Mohammad Marufuzzaman, Mark A Tschopp, and Linkan Bian. Porosity prediction: Supervised-learning of thermal history for direct laser deposition. *Journal of manufacturing systems*, 47:69–82, 2018.

[19] Mojtaba Khanzadeh, Sudipta Chowdhury, Mark A Tschopp, Haley R Doude, Mohammad Marufuzzaman, and Linkan Bian. In-situ monitoring of melt pool images for porosity prediction in directed energy deposition processes. *IISE Transactions*, 51(5):437–455, 2019.

[20] Wei Li, Jingwei Zhang, Xinchang Zhang, and Frank Liou. Effect of optimizing particle size on directed energy deposition of functionally graded material with blown pre-mixed multi-powder. *Manufacturing letters*, 13:39–43, 2017.

[21] Zuo Li, Shang Sui, Xu Ma, Hua Tan, Chongliang Zhong, Guijun Bi, Adam T Clare, Andres Gasser, and Jing Chen. High deposition rate powder-and wire-based laser directed energy deposition of metallic materials: A review. *International Journal of Machine Tools and Manufacture*, page 103942, 2022.

[22] Weiping Liu and JN Dupont. In-situ reactive processing of nickel aluminides by laser-engineered net shaping. *Metallurgical and materials transactions A*, 34:2633–2641, 2003.

[23] Zhibo Luo and Yaoyao Zhao. A survey of finite element analysis of temperature and thermal stress fields in powder bed fusion additive manufacturing. *Additive Manufacturing*, 21:318–332, 2018.

[24] Marco Mazzarisi, Sabina Luisa Campanelli, Andrea Angelastro, Fania Palano, and Michele Dassisti. In situ monitoring of direct laser metal deposition of a nickel-based superalloy using infrared thermography. *The International Journal of Advanced Manufacturing Technology*, 112:157–173, 2021.

[25] Ludwig Michalski, Krystyna Eckersdorf, J Kucharski, and J McGhee. *Temperature measurement*. John Wiley & Sons, 2001.

[26] RJ Moat, AJ Pinkerton, L Li, PJ Withers, and M Preuss. Residual stresses in laser direct metal deposited waspaloy. *Materials Science and Engineering: A*, 528(6):2288–2298, 2011.

[27] Mojtaba Mozaffar, Ebot Ndip-Agbor, Stephen Lin, Gregory J Wagner, Kornel Ehmann, and Jian Cao. Acceleration strategies for explicit finite element analysis of metal powder-based additive manufacturing processes using graphical processing units. *Computational Mechanics*, 64:879–894, 2019.

[28] Wook Jin Oh, Wook Jin Lee, Min Seob Kim, Jong Bae Jeon, and Do Sik Shim. Repairing additive-manufactured 316l stainless steel using direct energy deposition. *Optics & Laser Technology*, 117:6–17, 2019.

[29] AJ Pinkerton and L Li. Rapid prototyping using direct laser deposition—the effect of powder atomization type and flowrate. *Proceedings of the Institution of Mechanical Engineers, Part B: Journal of Engineering Manufacture*, 217(6):741–752, 2003.

[30] Andrew J Pinkerton and Lin Li. Modelling the geometry of a moving laser melt pool and deposition track via energy and mass balances. *Journal of Physics D: Applied Physics*, 37(14):1885, 2004.

[31] Dong Jin Ryu, Chung-Hee Sonn, Da Hee Hong, Kyeu Back Kwon, Sang Jun Park, Hun Yeong Ban, Tae Yang Kwak, Dohyung Lim, and Joon Ho Wang. Titanium porous coating using

3d direct energy deposition (ded) printing for cementless tka implants: does it induce chronic inflammation? *Materials*, 13(2):472, 2020.

[32] M Schmidt, R Kolleck, A Grimm, R Veit, and K Bartkowiak. Direct laser deposition of cu alloy on forming tool surfaces—process window and mechanical properties. *CIRP annals*, 59(1):211–214, 2010.

[33] Jan Schwerdtfeger, Robert F Singer, and Carolin Körner. In situ flaw detection by ir-imaging during electron beam melting. *Rapid Prototyping Journal*, 18(4):259–263, 2012.

[34] Kamran Shah, Izhar ul Haq, Ashfaq Khan, Shaukat Ali Shah, Mushtaq Khan, and Andrew J Pinkerton. Parametric study of development of inconel-steel functionally graded materials by laser direct metal deposition. *Materials & Design (1980-2015)*, 54:531–538, 2014.

[35] Nima Shamsaei, Aref Yadollahi, Linkan Bian, and Scott M Thompson. An overview of direct laser deposition for additive manufacturing; part ii: Mechanical behavior, process parameter optimization and control. *Additive Manufacturing*, 8:12–35, 2015.

[36] Alex Sherstinsky. Fundamentals of recurrent neural network (rnn) and long short-term memory (lstm) network. *Physica D: Nonlinear Phenomena*, 404:132306, 2020.

[37] Ziyad Smoqi, Benjamin D Bevans, Aniruddha Gaikwad, James Craig, Alan Abul-Haj, Brent Roeder, Bill Macy, Jeffrey E Shield, and Prahalada Rao. Closed-loop control of meltpool temperature in directed energy deposition. *Materials & Design*, 215:110508, 2022.

[38] Lijun Song, Vijayavel Bagavath-Singh, Bhaskar Dutta, and Jyoti Mazumder. Control of melt pool temperature and deposition height during direct metal deposition process. *The International Journal of Advanced Manufacturing Technology*, 58:247–256, 2012.

[39] Lijun Song and Jyoti Mazumder. Feedback control of melt pool temperature during laser cladding process. *IEEE Transactions on control systems technology*, 19(6):1349–1356, 2010.

[40] ASTM Standard et al. Standard terminology for additive manufacturing technologies. *ASTM International F2792-12a*, pages 1–9, 2012.

[41] Yuwen Sun and Mingzhong Hao. Statistical analysis and optimization of process parameters in ti6al4v laser cladding using nd: Yag laser. *Optics and Lasers in Engineering*, 50(7):985–995, 2012.

[42] Lie Tang and Robert G Landers. Melt pool temperature control for laser metal deposition processes—part i: Online temperature control. *Journal of manufacturing science and engineering*, 132(1), 2010.

[43] Scott M Thompson, Linkan Bian, Nima Shamsaei, and Aref Yadollahi. An overview of direct laser deposition for additive manufacturing; part i: Transport phenomena, modeling and diagnostics. *Additive Manufacturing*, 8:36–62, 2015.

[44] Trumpf.com, DLD applications. Ded application in manufacturing.

[45] Liang Wang, Sergio D Felicelli, and Phillip Pratt. Residual stresses in lens-deposited aisi 410 stainless steel plates. *Materials Science and Engineering: A*, 496(1-2):234–241, 2008.

[46] Sarah J Wolff, Samantha Webster, Niranjan D Parab, Benjamin Aronson, Benjamin Gould, Aaron Greco, and Tao Sun. In-situ observations of directed energy deposition additive manufacturing using high-speed x-ray imaging. *Jom*, 73:189–200, 2021.

[47] W Wu, LY Hwu, DY Lin, and JL Lee. The relationship between alloying elements and retained austenite in martensitic stainless steel welds. *Scripta Materialia*, 42(11):1071–1076, 2000.

[48] Yuhong Xiong, William H Hofmeister, Zhao Cheng, John E Smugeresky, Enrique J Lavernia, and Julie M Schoenung. In situ thermal imaging and three-dimensional finite element modeling of tungsten carbide–cobalt during laser deposition. *Acta materialia*, 57(18):5419–5429, 2009.

[49] Lei Yan, Xueyang Chen, Yunlu Zhang, Joseph W Newkirk, and Frank Liou. Fabrication of functionally graded ti and γ-tial by laser metal deposition. *Jom*, 69:2756–2761, 2017.

[50] Qingcheng Yang, Pu Zhang, Lin Cheng, Zheng Min, Minking Chyu, and Albert C To. Finite element modeling and validation of thermomechanical behavior of ti-6al-4v in directed energy deposition additive manufacturing. *Additive Manufacturing*, 12:169–177, 2016.

[51] Jiayu Ye, Alireza Bab-Hadiashar, Reza Hoseinnezhad, Nazmul Alam, Alejandro Vargas-Uscategui, Milan Patel, and Ivan Cole. Predictions of in-situ melt pool geometric signatures via machine learning techniques for laser metal deposition. *International Journal of Computer Integrated Manufacturing*, pages 1–17, 2022.

[52] Kai Zeng, Deepankar Pal, and Brent Stucker. A review of thermal analysis methods in laser sintering and selective laser melting. In *2012 International Solid Freeform Fabrication Symposium*. University of Texas at Austin, 2012.

[53] Ziyang Zhang, Zhichao Liu, and Dazhong Wu. Prediction of melt pool temperature in directed energy deposition using machine learning. *Additive Manufacturing*, 37:101692, 2021.

[54] Gangxian Zhu, Anfeng Zhang, Dichen Li, Yiping Tang, Zhiqiang Tong, and Qiaopan Lu. Numerical simulation of thermal behavior during laser direct metal deposition. *The International Journal of Advanced Manufacturing Technology*, 55:945–954, 2011.